PREDICTING GLIOMA MOLECULAR SUBTYPE FROM DIFFUSION ANISOTROPY INDICES' DISTRIBUTIONS

by

Hande Halilibrahimoğlu

B.S., in Medical Engineering, Acıbadem Mehmet Ali Aydınlar University, 2019

Submitted to the Institute of Biomedical Engineering
in partial fulfillment of the requirements
for the degree of
Master of Science
in
Biomedical Engineering

Boğaziçi University
2021

PREDICTING GLIOMA MOLECULAR SUBTYPE FROM DIFFUSION ANISOTROPY INDICES' DISTRIBUTIONS

APPROVED BY:

Assoc. Prof. Dr. Alpay Özcan .....
(Thesis Advisor)

Assoc. Prof. Dr. Esin Öztürk Işık .....

Asst. Prof. Engin Baysoy .....

DATE OF APPROVAL: 9 July 2021

ACKNOWLEDGMENTS

I would like start by thanking my thesis advisor Assoc. Prof. Dr. Alpay Özcan for his guidance, mentorship and advice, which still shapes my career. I also would like to thank Assoc. Prof. Dr. Esin Öztürk Işık for giving me the opportunity to work with her and her team as well as her valuable advice. I would like to thank Prof. Dr. Alp Dinçer for his support and time he took to answer my questions during this study. I would like to thank Asst. Prof. Engin Baysoy for his contributions to my career and for taking the time to be in my defense committee. I would also like to offer my thanks to Prof. Dr. Koray Özduman and Prof. Dr. Necmettin Pamir for their contributions.

I would to thank Korhan Polat, Seda Keskin, Ozan Genç and for their contributions and time for answering my questions. I would also like to thank my colleagues at the Computational Imaging Laboratory for their support and friendship. I would also like to thank my friends for their support and understanding during my studies.

Most importantly, I want to thank my family for their endless support, curiosity and understanding. I would also like to thank my uncle İskender Kosova for being a great role model and my mother Funda Kosova and grandmother Olsun Kosova for their endless support and curiosity during my journey in research.

This study has been funded by The Scientific and Technological Research Council of Turkey (TÜBİTAK) 1003 Grant No: 216S432.

ACADEMIC ETHICS AND INTEGRITY STATEMENT

I, Hande Halilibrahimoğlu, hereby certify that I am aware of the Academic Ethics and Integrity Policy issued by the Council of Higher Education (YÖK) and I fully acknowledge all the consequences due to its violation by plagiarism or any other way.

Name : Signature:

Date:

ABSTRACT

PREDICTING GLIOMA MOLECULAR SUBTYPE FROM DIFFUSION ANISOTROPY INDICES' DISTRIBUTIONS

Incorporation of glioma genetic mutations, including isocitrate dehydrogenase (IDH) and telomerase reverse transcriptase (TERT), provides information on overall survival and disease course. However, such mutations are determined from a biopsy sample which represent only the biopsied region. Non–invasive tumor genotype prediction have been studied, but they mostly focusing only on the tumor. Yet, gliomas are known to infiltrate along normal–appearing white matter (NAWM), where relevant genotype information might be available. Diffusion anisotropy indices (DAIs) and diffusion tensor eigenvalues (DTEs), derived from diffusion tensor imaging (DTI), can be used to quantify the diffusion in the NAWM of glioma patients with varying mutation status. We hypothesize that using full–distributions of DAIs and DTEs can better represent the complex tumor effects in the NAWM in comparison to usual summary statistics. In this study, we have compared the predictive values of summary statistics, full distributions and multi–Gaussian fitting (MGF) parameters of DAIs and DTEs in the NAWM for predicting IDH–TERT subgroups, IDH and TERT mutations in 70 glioma patients. Hemispheric variations were also investigated with hemisphere difference distributions.The results show that, full distributions can predict tumor genotype better than standard distribution parameters, and perform better than or as well as MGF parameters. Additionally, feature selection applied to full distributions further increased classification accuracy. IDH–TERT subgroups were best predicted with 78.6% accuracy, IDH mutation with 94.3% accuracy, and TERT mutation with 88.6% accuracy. In conclusion, full distributions are better predictors of genotype prediction. Future work will focus on increasing accuracy on a larger cohort and personalized MGF.

Keywords: Glioblastoma, Magnetic Resonance Imaging, Diffusion, Diffusion Tensor Imaging, Anisotropy Indices, Distributions, Machine Learning.

ÖZET

GLİOMLARDA GENETİK ALTGRUPLARIN DİFÜZYÖN EŞYÖNSÜZLÜK İNDİSLERİNİN DAĞILIMLARI İLE BELİRLENMESİ

İzositrat dehgidrogenaz (IDH) ve telomeraz ters transkriptaz (TERT) gibi gliom genetik mutasyonları sağkalım ve hastalığın seyri ile ilgili önemli bilgiler içerir. Ancak mutasyon tespiti yalnızca sınırlı bir bölgeyi temsil eden biyopsi örneği ile gerçekleştirilir. Literatürde invazif olmayan yöntemlerle mutasyon tespiti yapmayı amaçlayan çalışmalar bulunmaktadır, ancak bu çalışmaların çoğu yalnızca tümör bölgesi üzerine odaklanmıştır. Gliomlar normal görunen beyaz maddeyi (NGMB) istila etmeleriyle bilinirler. Bu yüzden bu bölgede genetik mutasyon tahmini icin gerekli bilgiler bulunabilir. Difüzyon tensör görüntülemeden (DTG) elde edilen difüzyön eşyönsüzlük indisleri (DEİ) ve difüzyon tensör özdeğerleri (DTÖ) bu bölgedeki difüzyonu tanımlamakta kullanılabilir. Tam DEİ ve DTÖ dağılımları, tümörun NGBM'deki kompleks etkilerini betimleyici istatistiklerden daha iyi temsil edebilir. Bu çalışmada, NGBM'deki DEİ ve DTÖlerin betimleyici istatistiklerinin, tam dağılımlarının ve çoklu–Gauss modeli (ÇGM) parametrelerinin IDH–TERT altgrupları ile IDH ve TERT mutasyonlarını tahmin etme performansları 70 gliom hastasında karsılaştırılmıştır. Beyin yarımküreleri arasındaki farklar ise sağlıklı ve tümörlü beyin yarımküre dağılımlarının farkı ile incelenmiştir. Sonuçlar tam DEİ ve DTÖ dağılımlarının gliom mutasyonlarını betimleyici istatistiklerden daha iyi, ÇGM parametrelerinden ise daha iyi ya da benzer performansta tahmin ettiğini göstermiştir. Aynı zamanda, öznitelik seçme yöntemleri sınıflandırma doğruluğunu arttırmıştır. IDH–TERT altgrupları en iyi %78.6, IDH mutasyonu en iyi %94.3 ve TERT mutasyonu en iyiy %88.6 doğruluk oranları ile tahmin edilmiştir. Gelecek çalışmalar sınıflandırma doğruluğunu arttırmaya ve hasta bazında ÇGM parametrelerinin değerlendirilmesine odaklanacaktır.

Anahtar Sözcükler: Glioblastom, Manyetik Rezonans Görüntüleme, Difüzyon Tensör Görüntüleme, Eşyönsüzlük İndisleri, Dağılımlar, Makine Öğrenmesi.

TABLE OF CONTENTS

ACKNOWLEDGMENTS iii
ACADEMIC ETHICS AND INTEGRITY STATEMENT iv
ABSTRACT v
ÖZET vi
LIST OF FIGURES ix
LIST OF TABLES xii
LIST OF SYMBOLS xv
LIST OF ABBREVIATIONS xvi
1. INTRODUCTION 1
2. LITERATURE REVIEW 7
3. PROBLEM STATEMENT 10
4. MATERIALS AND METHODS 11
4.1 Patient Characteristics 11
4.2 MRI Data Acquisition 13
4.3 NAWM Segmentation and Co–Registration 13
4.4 Data Preparation 15
4.5 Feature Selection and Extraction 16
4.5.1 Variance Threshold 17
4.5.2 Sequential Feature Selection 17
4.5.3 Singular Value Decomposition 18
4.6 Distribution Parameters and Multimodal Gaussian Fitting 19
4.7 Dimensionality Comparison of MGF in mRMSE and SVD 21
4.8 Statistical Analysis and Machine Learning 22
4.8.1 Statistical Analysis 22
4.8.2 Machine Learning 22
4.8.2.1 Decision Trees 23
4.8.2.2 Support Vector Machines 24
4.8.2.3 k-Nearest Neighbors 24
4.8.2.4 Ensemble Methods 24

4.8.2.5 Performance Evaluation 25
5. RESULTS 26
5.1 Statistical Analysis 26
5.2 MGF Dimensionality Selection 31
5.3 Machine Learning Results 32
5.3.1 Comparison of Distribution Representations 32
5.3.1.1 Effect of NAWM Hemisphere 36
5.3.2 Feature Selection Applied to Full Distributions 41
5.3.3 Dimensionality Comparison in MGF 46
6. DISCUSSION 52
7. CONCLUSION 57
8. List of publications produced from the thesis 58
APPENDIX A. NAWM Mask Registration 59
APPENDIX B. Definitions of Distribution Parameters 60
B.1 Mean 60
B.2 Standard Deviation 60
B.3 Median 60
B.4 Skewness 60
B.5 Kurtosis 61
B.6 p^{th} Percentile 61
REFERENCES 62

LIST OF FIGURES

Figure 1.1 Magnitude and shape of water diffusion in (A) isotropic medium and (B) anisotropic medium. In (A) isotropic medium, water diffusion is equal in magnitude along all major orthogonal axis, thus forming a sphere. In (B) anisotropic medium, water diffusion is stronger in one direction and forms an ellipse. 5

Figure 4.1 Distributions of (A) IDH–TERT subgroup labels, (B) IDH mutation status, (C) TERT mutation status. 12

Figure 4.2 NAWM segmentations and masks. (A) T_2W image, (B) NAWM segmentation overlaid on T_2W image, (C) co–registered B_0 image, (D) NAWM segmentation on co–registered B_0 image, (E) total NAWM mask on T_2W image, (F) on B_0 image and corresponding (G) right and (H) left hemisphere masks. 14

Figure 4.3 Whole brain NAWM (A) ADC, (B) FA, (C) RA, (D) λ_1, (E) λ_2, (F) λ_3 distributions and multimodal Gaussian fits of an example patient. Gray area: 1000-bin distribution. Red line: Multimodal Gaussian fit. 19

Figure 5.1 Boxplots of whole brain NAWM (A) ADC and DTE medians and (B) FA and RA medians grouped by IDH–TERT subgroups, (C) ADC and DTE medians and (D) FA and RA medians grouped by IDH mutation, (E) ADC and DTE medians and (F) FA and RA medians grouped by TERT mutation status. * indicate statistical significance < 0.05, $*$ indicate statistical significance < 0.0085 according to Dunn–Sidak correction for post-hoc analysis. 27

Figure 5.2 Boxplots of hemisphere difference (A) ADC and DTE medians and (B) FA and RA medians grouped by IDH–TERT subgroups, (C) ADC and DTE medians and (D) FA and RA medians grouped by IDH mutation, (E) ADC and DTE medians and (F) FA and RA medians grouped by TERT mutation status. * indicate statistical significance < 0.05, *$*$ indicate statistical significance < 0.0085 according to Dunn–Sidak correction for post-hoc analysis. 30

Figure 5.3 Validation accuracy comparison of whole brain NAWM and hemisphere difference full DAI and DTE distributions, distribtuion parameters and MGF parameters selected with mRMSE in (A–B) IDH–TERT subgroups, (C–D) IDH mutation, (E–F) TERT mutation classifications.MGF parameters were analyzed as contralateral and ipsilateral hemisphere for hemipshere difference analysis. 33

Figure 5.4 Validation accuracy comparison of the full whole brain NAWM and hemisphere difference DAI and DTE distributions for (A) IDH–TERT subgroups, (B) IDH mutation, and (C) TERT mutation classifications. 38

Figure 5.5 Validation accuracy comparison of the whole brain NAWM and hemisphere difference DAI and DTE distribution parameters for (A) IDH–TERT subgroups, (B) IDH mutation, and (C) TERT mutation classifications. 39

Figure 5.6 Validation accuracy comparison of the whole brain, contralateral, ipsilateral NAWM DAI and DTE MGF parameters for (A) IDH–TERT subgroups, (B) IDH mutation, and (C) TERT mutation classifications. 40

Figure 5.7 Validation accuracy comparison of feature selection methods applied to full whole brain NAWM and hemisphere difference DAI and DTE distributions in (A–B) IDH–TERT subgrops, (C–D) IDH mutation, (E–F) TERT mutation classifications. 42

Figure 5.8 Validation accuracy comparison of DAI and DTE MGF parameters of whole brain, contralateral and ipsilateral NAWM whose components were selected with mRMSE and SVD in (A–C) IDH–TERT subgroups, (D–F) IDH mutation, (G–I) TERT mutation classifications. 46

Figure A.1 Detailed steps of NAWM mask registration using in–house MATLAB® software. (A) T_2W image, (B) NAWM mask delineated in T_2W image space and (C) segmetation mask, (D) T_2W image, (E) B_0 map registered to T_2W imge sapce using FSL, (F) overlay of NAWM mask in T_2W image space on $B_0 \rightarrow T_2W$ image, (G–I) whole brain, left and right hemisphere NAWM masks registered to B_0 image space using in–house developed MATLAB® software. 59

LIST OF TABLES

Table 4.1	Cohort Characteristics.	11
Table 5.1	Comparison of whole brain NAWM and hemipshere difference medians IDH–TERT molecular subgroups with Kruskal–Wallis test. * *indicates* $p < 0.05$.	26
Table 5.2	Comparison of whole brain NAWM hemipshere difference medians in IDH mutation status with Mann–Whitney U–test. * *indicates* $p < 0.05$.	28
Table 5.3	Comparison of whole brain NAWM hemipshere difference medians in TERT mutation status with Mann–Whitney U–test. * *indicates* $p < 0.05$	29
Table 5.4	mRMSE values of each Gaussian fit for each DAI and DTE. Boldfaced mRMSE values indicate the selected number of Gaussian sums.	31
Table 5.5	Number of selected Gaussian components with SVD and their corresponding mRMSE for each DAI and DTE.	32
Table 5.6	Classification results with the highest validation accuracy in IDH–TERT subgroup prediction using full distributions, distribution parameters and MGF parameters where components were selected with mRMSE. **Due to the class imbalance between the 4 classes of IDH–TERT subgroups, one of the class–wise precision calculations results in zero–division. This zero–division leads to NaN in averaged precision.*	34
Table 5.7	Classification results with the highest validation accuracy in IDH mutation prediction using full distributions, distribution parameters and MGF parameters where components were selected with mRMSE.	35

Table 5.8 Classification results with the highest validation accuracy in TERT mutation prediction using full distributions, distribution parameters and MGF parameters where components were selected with mRMSE. 37

Table 5.9 Classification results with the highest validation accuracy in IDH–TERT subgroup prediction using full whole brain NAWM DAI and DTE distributions without and with feature selection. 41

Table 5.10 Classification results with the highest validation accuracy in IDH–TERT subgroup prediction using full hemisphere difference DAI and DTE distributions without and with feature selection. 43

Table 5.11 Classification results with the highest validation accuracy in IDH mutation prediction using full whole brain NAWM DAI and DTE distributions without and with feature selection. 44

Table 5.12 Classification results with the highest validation accuracy in IDH mutation prediction using full hemisphere difference DAI and DTE distributions without and with feature selection. 44

Table 5.13 Classification results with the highest validation accuracy in TERT mutation prediction using full whole brain NAWM DAI and DTE distributions without and with feature selection. 45

Table 5.14 Classification results with the highest validation accuracy in TERT mutation prediction using full hemisphere difference DAI and DTE distributions without and with feature selection. 45

Table 5.15 Classification results with the highest validation accuracy in IDH–TERT subgroup prediction using MGF parameters of DAI and DTE distributions. Number of Gaussian components were selected with mRMSE. * *Due to the class imbalance between the 4 classes of IDH–TERT subgroups, one of the class–wise precision calculations results in zero–division. This zero–division leads to NaN in averaged precision.* 47

Table 5.16 Classification results with the highest validation accuracy in IDH–TERT subgroup prediction using MGF parameters of DAI and DTE distributions. Number of Gaussian components were selected with SVD using 20% relative change threshold. * *Due to the class imbalance between the 4 classes of IDH–TERT subgroups, one of the class–wise precision calculations results in zero–division. This zero–division leads to NaN in averaged precision.* 47

Table 5.17 Classification results with the highest validation accuracy in IDH mutation prediction using MGF parameters of DAI and DTE distributions. Number of Gaussian components were selected with mRMSE. 48

Table 5.18 Classification results with the highest validation accuracy in IDH mutation prediction using MGF parameters of DAI and DTE distributions. Number of Gaussian components were selected with SVD using 20% relative change threshold. 49

Table 5.19 Classification results with the highest validation accuracy in TERT mutation prediction using MGF parameters of DAI and DTE distributions. Number of Gaussian components were selected with mRMSE. 50

Table 5.20 Classification results with the highest validation accuracy in TERT mutation prediction using MGF parameters of DAI and DTE distributions. Number of Gaussian components were selected with SVD using 20% relative change threshold. 50

LIST OF SYMBOLS

A	Original data matrix
a	Amplitude of a Gaussian component
b	Location or centroid of a Gaussian component
c	Width of a Gaussian component
d	Coefficients of the Gaussian function
g	Total number of classes
D	Diffusion tensor
E	Diffusion tensor eigenvalues
$F(a, x)$	Fitted vector or matrix–valued multimodal Gaussian function
h_k	Distribution of the kth patient
$\bar{h}_k$	Density function of the kth patient
$\hat{h}_k$	Mean–centered density function of the kth patient
$I\{\hat{y}_j \neq y_j\}$	Indicator function
K	Total number of patients
l	Bin index
m	Total number of bins in the distribution
$\mu_{\bar{H}}$	Mean of the distribution bins calculated over the cohort
N_k	k^{th} patient's total number of mask pixels
n	Number of Gaussian components
Σ, σ	Singular value matrix and singular value
U, u	Left singular vectors
V, v	Right singular values
x	Input feature
y	Multimodal Gaussian function
$\hat{y}$	Observed or ground truth data
x	Input distribution
$\hat{z}$	Minmax scaled input feature

LIST OF ABBREVIATIONS

2–HG	2–hydroxygluterate
α–KG	α–ketogluterate
ADC	Apparent Diffusion Coefficient
CNS	Central Nervous System
DAI	Diffusion Anisotropy Indices
DICOM	Digital Imaging and Communications in Medicine
DTE	Diffusion Tensor Eigenvalues
DTI	Diffusion Tensor Imaging
FA	Fractional Anisotropy
FN	False Negative
FP	False Positive
FSL	Oxford University FMRIB Software Library
GDCM	Grassroots DICOM Library
HIF–1α	Hypoxia Inducible Factor–1α
IDH	Isocitrate Dehydrogenase
IDHmut	IDH–mutant
IDHwt	IDH–wildtype
kNN	k–Nearest Neighbors
MD	Mean Diffusivity
MGF	Multimodal Gaussian Fitting
MIPAV	Medical Image Processing, Analysis, and Visualization
MLA	Machine Learning Algortihm
MRI	Magnetic Resonance Imaging
mRMSE	Mean Root Mean Square Error
MRS	Magnetic Resonance Spectroscopy
NAA	N-acetylaspartate
NADPH	Nicotinamide Adenine Dinucleotide Phosphate
NAWM	Normal–Appearing White Matter

NifTI	Neuroimaging Informatics Technology Initiative
RA	Relative Anisotropy
RMSE	Root Mean Square Error
ROI	Region of Interest
RUS	Random Undersampling
SBFS	Sequential Backward Feature Selection
SFFS	Sequential Forward Feature Selection
SVD	Singular Value Decomposition
SVM	Support Vector Machine
T_1W	T_1–weighted
T_2W	T_2–weighted
TERT	Telomerase Reverse Transcriptase
TERTmut	TERT–mutant
TERTwt	TERT–wildtype
TN	True Negative
TP	True Positive
WHO	World Health Organization

1. INTRODUCTION

Glioma is the most common central nervous system (CNS) tumor, constituting more than 70% of all malignant CNS tumors [1]. Standard of care treatment consists of surgical resection, radiotherapy and chemotherapy [2]. Yet, survival remains poor with 12–15 months for glioblastomas, which constitutes more than 50% of all malignant gliomas. For other gliomas survival can extend to 5 or more years depending tumor type [1]. Decisions on treatment options become highly relevant for establishing a balance between patient comfort and life span, e.g., opting for surgery is based on expected survival times. In the past, gliomas were classified into grades by histopathology, with larger grade number corresponding to a more aggressive tumor [3]. While this was the main decision factor for disease classification in the past, more recently, use of glioma genotype information in clinical workflow has shown to be valuable in prognosis and treatment response evaluation [4], which led to the integration of glioma genetic alterations to World Health Organization (WHO) 2016 tumor classification system [5]. Isocitrate dehydrogenase (IDH) mutation is one of the classification criterion used by WHO 2016 tumor classification system. In addition, mutation in telomerase reverse transcriptase (TERT) informs clinicians on tumor aggressiveness and disease course.

IDH enzymes are responsible for the production of nicotinamide adenine dinucleotide phosphate (NADPH) and α–ketogluterate (α–KG) in cells. While, NADPH is used in multiple cellular processes including cell division and reduction of oxidative stress, α–KG is utilized in the energy metabolism. On the other hand, mutant IDH gene, first identified in gliomas by Parsons et al. [6], produces mutant IDH enzymes which further convert α-KG to 2–hydroxyglutarate (2–HG) [7]. Accumulation of 2–HG in the cell eventually alters cell differentiation mechanisms and cause tumor formation. Furthermore, 2–HG accumulation also causes a cascade of events that decreases hypoxia–inducible factor 1α (HIF–1α), which is responsible for oxygen consumption and suppression of the production of reactive oxygen species that might harm the cell. With a decrease in HIF–1α, the cell becomes prone to oxidative damage. In contrast,

HIF–1α is also activated in gliomas, increasing tumor cell proliferation and angiogenesis. It is hypothesized that activation of HIF–1α and IDH mutation in gliomas increase tumor cell proliferation, but also make cell susceptible to damage, which is an advantage because it might explain why IDH–mutant (IDHmut) gliomas have more favorable outcome [8].

TERT gene regulates the expression of TERT, a catalyzer for the enzyme telomerase which maintains the length of telomeres in the cell. Without telomerase activity, proliferation capabilities of the cells slowly diminishes as telomeres shorten with each cell division. Telomerase enzyme prevents telomere shortening and is expressed during development. In cancer, TERT gene can be overexpressed as a result of a mutation, leading to increased telomerase activity, which is believed to be a precursor for glioma cell formation as cells gain immortality [4, 9, 10]. However, the biology of TERT mutation and its effects are still being investigated.

IDH mutation is more common in secondary glioblastomas and low–grade (grade II and grade III) gliomas and are associated with higher overall survival of 57 months [4, 6, 11, 12, 13]. Mutation of the TERT gene is usually seen in high–grade (grade IV) gliomas and primary glioblastomas, and their presence is associated with the worst lower overall survival of 11.5 months [4, 9]. On the other hand, overall survival increases to 125 months when both IDH and TERT mutations are present.

Histopathological and genetic information obtained from biopsy [2] can only cover targeted area, which, is prone to increased false negative rates due to highly challenging tumor heterogeneity [14]. In contrast, magnetic resonance imaging (MRI) can offer a non–invasive alternative to biopsy by providing information from a larger area while decreasing sampling bias and increasing patient comfort. Accordingly, current MRI radiomics research has focused on the analysis of observer placed or segmented tumor's region of interest (ROI) [15, 16, 17, 18] with the aim of identifying glioma genotypes without biopsy. However, gliomas' notoriously heterogeneous landscape [14] might affect the whole brain in a diffuse manner rather than remaining in tumor locus. This raises the concern that diffuse, rather than focal, tissue properties,

which might potentially be crucial in genotype identification and thereby disease staging and/or clinical decisions, are left unexamined with biopsy and/or MRI tumor ROI analysis [19].

For instance, a crucial diffuse characteristic is glioma's tendency to infiltrate into normal appearing white matter (NAWM) [19, 20, 21]. The infiltrative behavior of gliomas were first shown by Hans–Joachim Scherer [20] almost a century ago. His research showed that gliomas prefer to infiltrate along pre–existing structures, such as white matter fibers, also confirmed by modern research [22, 23]. His research showed that a large majority of gliomas exhibited infiltrative growth, with the exception of ependymomas which sharp and clear tumor borders. Among those gliomas exhibiting infiltrative growth, not all tumors destroy the brain parecnyhma (i.e white matter fibres) followed during migration. Destruction of the brain tissue was observed in glioblastomas [24]. In the following decades, research into the biological mechanisms of glioma infiltration has shown complex interactions of tumor cells with extra-cellular matrix components and cytokines [25].

By providing a methodology for whole brain coverage, MRI might be useful in investigating the infiltrative nature of gliomas specifically in NAWM. However, anatomical MRI, such as T_1–weighted (T_1W) and T_2–weighted (T_2W) contrast mechanisms, might not be sufficiently sensitive to NAWM infiltration [21], especially at the early disease stages [26]. By contrast, microstructural changes in NAWM have the potential to present relevant information for glioma infiltration.

Investigating and quantifying microstructural changes in NAWM is realized by diffusion MRI, most popularly with Diffusion Tensor Imaging (DTI) [27]. In brief, DTI is composed of diffusion-weighted images acquired from multiple directions. Signal attenuation depends on the restricted movement of water molecules, which is shaped by the underlying tissue microstructure, for each diffusion-weighted image. Signal attenuates faster during free diffusion, due to higher decrease in the MRI signal. The DTI model calculates at each pixel three eigenvalues of the diffusion tensor which represent diffusitivities in the three orthogonal major motion directions, i.e. in the

coordinate frame defined by the tensor's eigenvectors, whereby providing an orientation independent characterization of local microstructure.

The diffusion tensor consists of 2 components; eigenvectors (D) and eigenvalues (E) that represent the direction and magnitude of movement, respectively.

$$D = \begin{bmatrix} D_{xx} & D_{xy} & D_{xz} \\ D_{yx} & D_{yy} & D_{yz} \\ D_{zx} & D_{zy} & D_{zz} \end{bmatrix} \tag{1.1}$$

$$E = \begin{bmatrix} \lambda_1 & 0 & 0 \\ 0 & \lambda_2 & 0 \\ 0 & 0 & \lambda_3 \end{bmatrix} \tag{1.2}$$

Elements of matrix D corresponds to the eigenvectors of the diffusion tensor, which represents the coordinates of the diffusion ellipse in space. Matrix E includes the eigenvectors of the diffusion matrix, which are positioned diagonally in descending order, such that $\lambda_1 > \lambda_2 > \lambda_3$. Elements of E corresponds to the length of each axis of the diffusion ellipse, or diffusivity along each major orthogonal direction.

Diffusion of water molecules in the tissue can be inferred from the diffusion ellipse. When diffusion is isotropic, water molecules move equally in all directions, all eigenvalues are equal ($\lambda_1 = \lambda_2 = \lambda_3$), thus diffusion ellipse is a sphere (Figure 1.1). When diffusion is anisotropic, water molecules moves preferentially along one direction, eigenvalues are not equal, which allows diffusion movement to be represented with an ellipse [28]. Diffusion anisotropy indices (DAIs), derived from diffusion tensor eigenvalues (DTEs), quantify the degree of anisotropy in tissues. While mean diffusivity (MD; or apparent diffusion coefficient, ADC) represents the mean diffusivity, as the

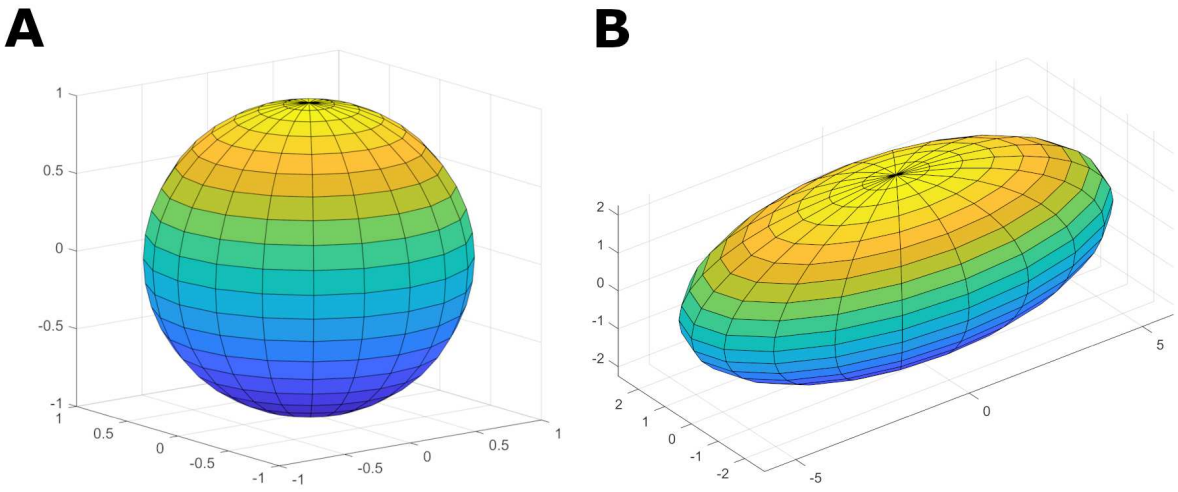

Figure 1.1 Magnitude and shape of water diffusion in (A) isotropic medium and (B) anisotropic medium. In (A) isotropic medium, water diffusion is equal in magnitude along all major orthogonal axis, thus forming a sphere. In (B) anisotropic medium, water diffusion is stronger in one direction and forms an ellipse.

mean of eigenvalues, fractional anisotropy (FA) and relative anistoropy (RA) quantify the degree of anisotropy.

$$\text{ADC} = \frac{\lambda_1 + \lambda_2 + \lambda_3}{3} \tag{1.3}$$

$$\text{FA} = \frac{\sqrt{(\lambda_1 - \lambda_2)^2 + (\lambda_2 - \lambda_3)^2 + (\lambda_1 - \lambda_3)^2}}{\sqrt{2(\lambda_1^2 + \lambda_2^2 + \lambda_3^2)}} \tag{1.4}$$

$$\text{RA} = \frac{\sqrt{3((\lambda_1 - \lambda_2)^2 + (\lambda_2 - \lambda_3)^2 + (\lambda_1 - \lambda_3)^2)}}{\lambda_1 + \lambda_2 + \lambda_3} \tag{1.5}$$

DAIs and DTEs guarantee a direction independent estimation of microstructure thereby eliminating effects of white matter tissue displacements caused by the tumor volume and locus, e.g. in comparing infiltrative gliomas and non–infiltrative meningiomas. In the brain, anisotropic diffusion is mainly observed in the normal-appearing white matter due to the shape of axon fibers, whereas isotropic diffusion is observed in normal-appearing gray matter [28, 29].

Considering the highly infiltrating behavior of gliomas on top of tumor heterogeneity, DTI might represent the mutation–related effects of the tumor by investigating the NAWM. DAIs and DTEs, derived from DTI, are appropriate tools to investigate changes in the NAWM, with their sensitivity to motion of water in anisotropic tissue. Studies show that IDH and TERT mutations may have varying effects, proportional to tumor grade, which can be detected with DAIs and DTEs. Most studies in the literature use summary statistics, such as mean or percentile values, to correlate diffusion alterations in the NAWM with tumor related effects in a pre-defined ROI of the tumor or the NAWM. full distributions of DAIs and DTEs may have better predictive value for IDH and TERT mutation prediction.

2. LITERATURE REVIEW

An early study by Price et al. [30] investigated RA in tumor, peritumoral NAWM and contralateral NAWM of glioma patients. This study revealed RA abnormalities in regions with no T_2–abnormality and contralateral NAWM in high–grade glioma patients. RA decrease in NAWM regions with normal appearance on T_2W MRI was also reported. Later, Inglese et al. [31] reported decreased N-acetylaspartate (NAA), a neuronal marker, and increased MD in the contralateral NAWM, correlating magnetic resonance spectroscopy (MRS) and DTI parameters. Maudsley et al. [32] confirmed these findings and also reported metabolite changes occurring with a greater magnitude in higher grade gliomas. Goebell et al. [33] studied NAA and FA changes along tumor center, tumor border, peritumoral white matter and contralateral white matter, and showed decreasing neuronal integrity indicated by decreasing NAA and FA when moving towards tumor center. Kallenberg et al. [34] also found increased ADC and decreased FA in the NAWM glioma patients compared to controls, confirming previous findings. Provenzale et al. [35] compared ADC and FA changes in peritumoral T_2–hyperintense regions and peritumoral white matter among glioma and meningioma patients. Although no significant difference in ADC changes was found, a significant difference in FA decreases in the peritumoral white matter was found, where there were no abnormalities in T_2W MRI. However, a more recent study [36], while in accord with the earlier results, questions whether DAI changes are solely due to infiltration as it reports similar changes in meningioma, which is a non–infiltrative disease. Another study by Kassubek et al. [37] studied interhemispheric FA changes before and after radiation therapy to identify radiotherapy–related white matter damage. They found decreased global interhemispheric FA after radiation therapy, which could be a biomarker for radiation-induced white matter damage, and confirmed this finding with longitudinal data.

In addition, glioma infiltration and changes in DAI metrics were studied to correlate histopathology of tumor infiltration and imaging parameters as well. Specifically,

a study by Stadlbauer et al. [38] found a negative logarithmic correlation of FA with tumor cell number and negative linear correlation with percantage tumor infiltration. Furthermore, this study reported a positive logarithmic correlation of MD with tumor cell number and positive linear correlation with percent tumor infiltration. Another study by Deng et al. [39] aimed to correlate DTI parameters with tumor cell count obtained from peritumoral edematous tisse, in an attempt to quantitatively analyze glioma infiltration. The study reported increased ADC in peritumoral edematous region and a negative FA correlation with degree of infiltration.

Following the inclusion of tumor genetics in WHO 2016 classification system, effect of different mutations were also studied in the NAWM. Jütten et al. [40] investigated changes in MD, FA, axial and radial diffusivities in IDHmut and IDH–wildtype (IDHwt) patients. Notably, results demonstrated higher FA and lower MD, axial and radial diffusivities in IDHmut patients in comparison to IDHwt, which indicates white matter integrity. Their hypothesis of better prognosis in IDHmut patients was also confirmed by higher scores in cognitive function tests of IDHmut patients. In addition, IDHwt glioblastomas and lower grade gliomas have been shown to have less invasive phenotype measured with the isotropic and anisotropic components of the diffusion tensor [41, 42].

The aforementioned studies used standard histogram parameters, for instance mean and peak width, assuming diffusion anisotropy distributions were normally–distributed. Skew and kurtosis of ADC distributions were accounted for by analyzing the distributions as multi–Gaussian in the literature, however, no studies, so far, modeled DAI of NAWM as multi–Gaussians. For example, several studies [16, 43, 44, 45, 46, 47] modeled enhancing tumor ADC distributions as 2–component Gaussians using probabilistic Gaussian Mixture Modeling, and analyzed upper and lower ADC curves to predict progression–free and overall survival in recurrent glioblastoma patients. Similar approach was used by Huo et al. [48] to predict treatment response in glioblastoma patients.

Standard distribution parameters may not capture all the information inside a

ROI, considering the heterogeneity of gliomas. Studies using full diffusion anisotropy or eigenvalue distributions to study gliomas are limited and mostly encompass tumor region instead of NAWM. One study by Tozer et al. [15] investigated whether tumor ADC histograms could predict low–grade glioma subtypes. This study also compared the performance of standard histogram parameters, including peak height, peak location, mean, and percentile values, with raw ADC histogram, and concluded that raw histograms had better predictive value compared to standard histogram parameters. Another study by Lutz et al. [49] tested whether the shift in ADC histograms could differentiate patients with T_2–progress or stable disease. Their results showed ADC shift toward lower or higher values in T_2–progress compared to control group. Furthermore, distributions of patients with following T_1–progress had shifted toward lower ADC values, which suggested ADC shift may be time–dependent.

3. PROBLEM STATEMENT

Past studies were based mostly on straightforward statistics of NAWM ROIs such as the mean DAI values and/or histogram properties such as percentile points, peak height and location [15, 40]. If tumor heterogeneity affects NAWM microstructure, DAI distributions would be expected to be 'complicated' functions unlike, for instance, a Gaussian distribution function. This raises the concern that straightforward statistical parameters, such as mean ROI value and variance, might become less informative due to the averaging of various microstructure populations within the NAWM, e.g., distal versus proximal tissue.

In this study, the predictive value of usual summary statistics, multi–Gaussian fitting parameters, full distributions with different resolutions, and selected bins of full distributions of DAIs and DTEs were compared in predicting IDH–TERT subgroups, IDH mutation and TERT mutation. Feature selection and extraction techniques were used capture only the most informative subset of distribution bins for classification. In contrast to studies in literature, Gaussian curve fitting (multimodal Gaussian fitting, MGF) was utilized, instead of Gaussian Mixture Modeling, a probabilistic approach, to extract multi–Gaussian parameters. In addition, to analyze hemispheric variations, all distributions were calculated for whole brain NAWM and hemisphere difference of contralateral and ipsilateral NAWM. All features were used as inputs in machine learning algorithms (MLAs) for glioma molecular subgroup prediction.

4. MATERIALS AND METHODS

4.1 Patient Characteristics

Table 4.1
Cohort Characteristics.

Patient Demographics	
Mean Age ± SD	43.73 ± 15.32
Gender	30F/40M
Tumor Characteristics	
Tumor Grade	*Count (%)*
Grade I	1 (1%)
Grade II	29 (41%)
Grade III	22 (31%)
Grade IV	18 (26%)
IDH mutation (WT/MUT)	29/41 (41%/59%)
TERT mutation (WT/MUT)	33/37 (47%/53%)

In this institutional review board approved retrospective study, out of 170 consecutive glioma patients with written informed consent, data from 70 patients (age: 43.73 ± 15.32, F/M: 30/40) with full sets of T_2W images, DTI and, IDH and TERT data were analyzed. All patients were treated at Acıbadem Hospitals (Istanbul, Turkey) between March 2012 and February 2016. Histopathology analysis was performed on surgically removed tumor samples which were analyzed according to WHO 2016 Classification of Tumors of the Central Nervous System Scheme [5]. IDH and TERT mutations were determined using either minisequencing or Sanger sequencing [50].

Patients were further stratified into 4 molecular subgroups, from hereon, referred as IDH–TERT subgroups.:

1. **Double negative**: IDH–wildtype, TERT–wildtype ($n = 9$),

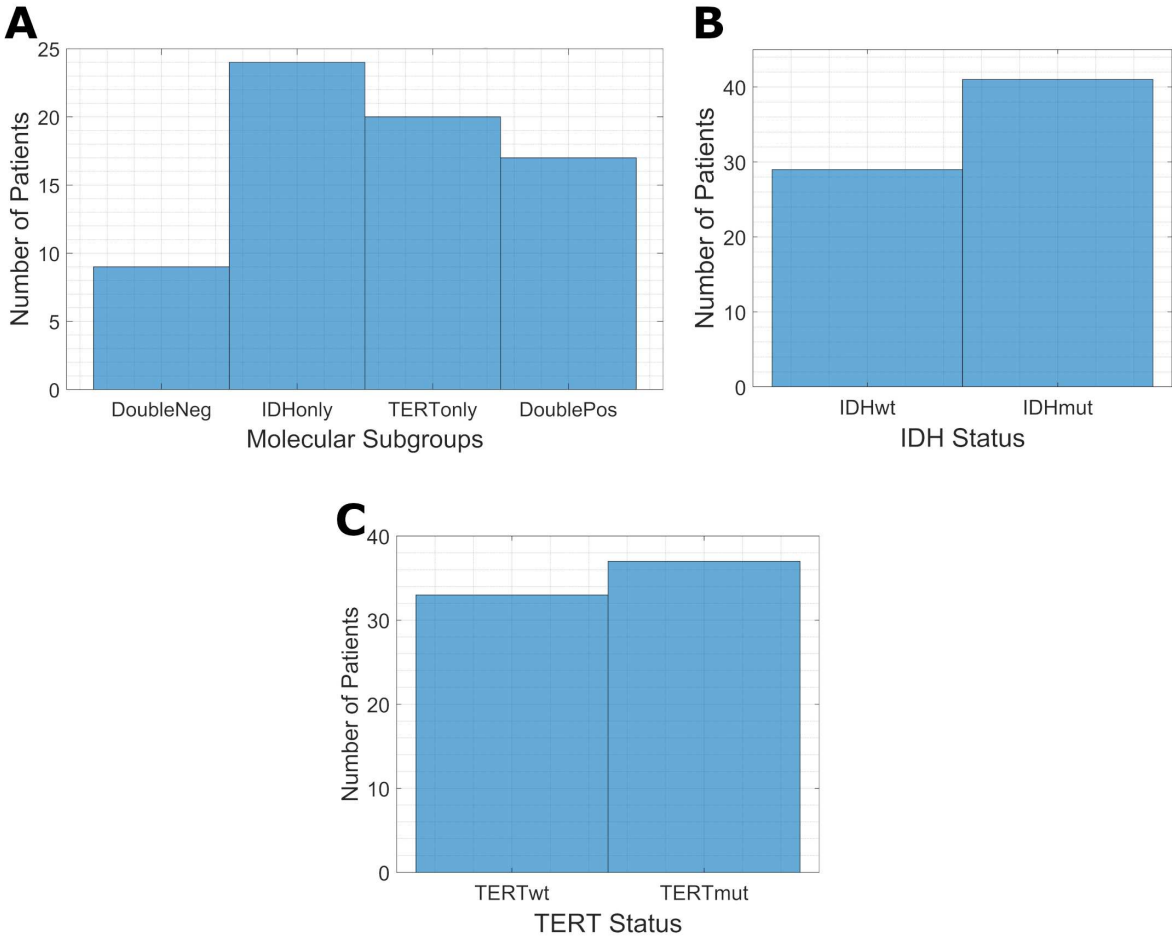

Figure 4.1 Distributions of (A) IDH–TERT subgroup labels, (B) IDH mutation status, (C) TERT mutation status.

2. **IDHonly**: IDH–mutant, TERT–wildtype ($n = 24$),

3. **TERTonly**: IDH–wildtype, TERT–mutant ($n = 20$),

4. **Double positive**: IDH–mutant, TERT–mutant ($n = 17$).

Cohort characteristics and demographics described by molecular subgrouping and histopathological grading are presented in Table 4.1, and mutation status distributions of IDH–TERT subgroups, IDH and TERT mutations are shown in Figure 4.1 Among the patients 1 (1%) had Grade I, 29 (41%) had Grade II, 22 (31%) had Grade III and 18 (26%) had Grade IV gliomas. 41 (59%) tumors were IDH-mutated (IDHmut), whereas 29 (41%) were IDH–wildtype (IDHwt). While 37 (53%) patients had TERT–mutant (TERTmut) tumors, 33 (47%) patients had TERT–wildtype tumors (TERTwt).

4.2 MRI Data Acquisition

MR imaging was conducted on a 3T Siemens Magnetom Tim Trio MR scanner (Siemens Healthineers, Erlangen, Germany) with a 32–channel head coil, 1 to 7 days before surgery. The scanning protocol included T_2W images acquired using $2D$ turbo spin echo sequence with voxel dimensions of $0.26 \times 0.26 \times 0.26$mm with 20 axial slices, $T_E/T_R = 107/3470$ms, slice thickness = 5mm, slice spacing = 6.5mm, flip angle = 120°. DTI data were acquired using $2D$ diffusion EPI sequence with $1.8 \times 1.8 \times 1.8$mm voxels, 60 axial slices, $T_E/T_R = 107/3470$ms, slice thickness = 1.8mm, slice spacing = 2.34mm, flip angle = 90° and b–value = 1000ms/mm^2 with 20 diffusion gradient vectors. DTI eigenvalue maps for the three eigenvalues ($\lambda_1 \geq \lambda_2 \geq \lambda_3$) were computed by the scanner's console computer.

All of the image volumes were transferred in Digital Imaging and Communications in Medicine (DICOM) format, which were then anonymized using in–house developed scripts based on Grassroots DICOM library (GDCM) [51]. The data were converted to Neuroimaging Informatics Technology Initiative (NIfTI) format using Medical Image Processing, Analysis, and Visualization (MIPAV) software [52]. For converting B_0 and eigenvalue images that were in 'mosaic' DICOM format, in–house developed MATLAB®(Mathworks Inc., Natick, MA, USA) software was used.

4.3 NAWM Segmentation and Co–Registration

NAWM regions were selected on T_2W images using semi–automatic level set segmentation tools in MIPAV by two trainees with 2 years of experience (Ozan Genç and Oğuzhan Aslan), inspected by an imaging scientist of 20+ years of experience (Alpay Özcan) and approved by a neuro–radiologist with 30+ years of experience (Alp Dinçer).

B_0 images were co–registered onto T_2W images with Oxford University FMRIB

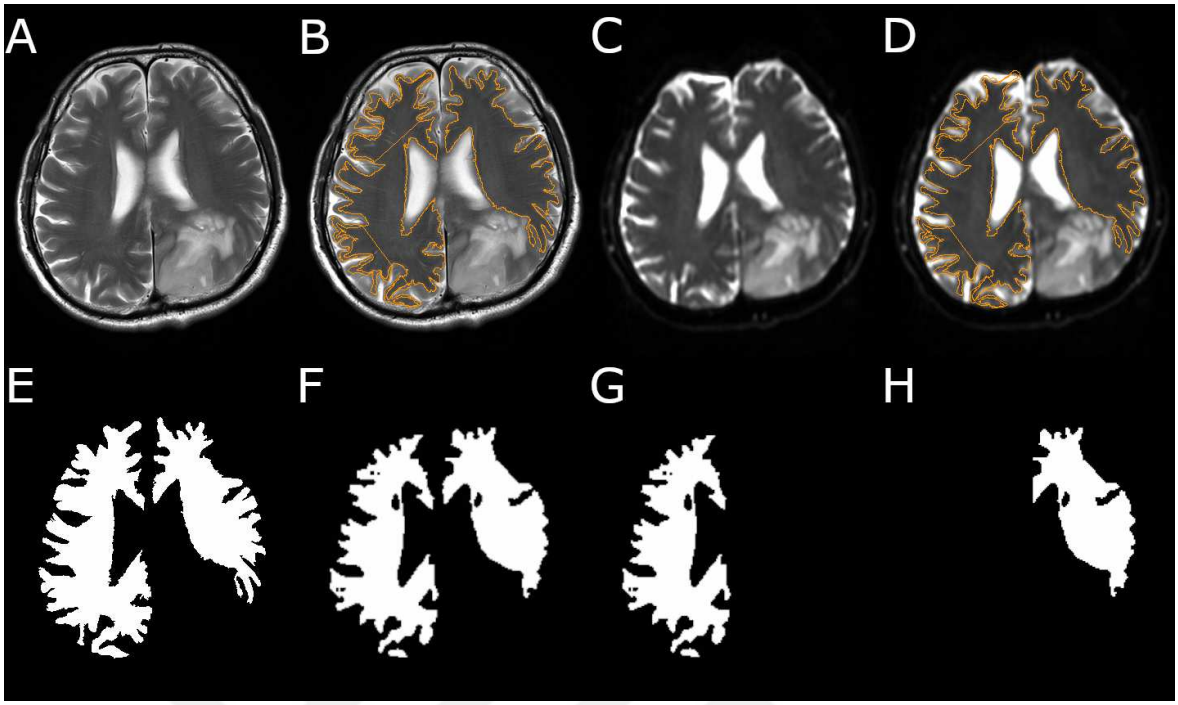

Figure 4.2 NAWM segmentations and masks. (A) T_2W image, (B) NAWM segmentation overlaid on T_2W image, (C) co–registered B_0 image, (D) NAWM segmentation on co–registered B_0 image, (E) total NAWM mask on T_2W image, (F) on B_0 image and corresponding (G) right and (H) left hemisphere masks.

Software Library (FSL) [53] using the mutual information cost function with trilinear interpolation method. The transformation optimizing the $B_0 \rightarrow T_2W$ co–registration problem was applied for co–registering eigenvalue maps onto T_2W images by interpolating with the nearest neighbor method for preventing 'invention' of data values.

The distortion of NAWM masks caused by the difference of total slice numbers between the MR modalities while co–registering was corrected with an in–house developed MATLAB® code[1] which identifies shared pixel coordinates in matching B_0 images mapped to T_2W images and the original B_0 image. The code infers mask pixels in the 'sandwich' slices from the 'shell' slices, and interpolates with nearest neighbor method.

Furthermore, an in–house developed MATLAB® code sub–divided the mask

[1]In-house mask registration and hemisphere separation programs were developed by Korhan Polat at Dr. Alpay Özcan's laboratory.

images automatically into left and right hemispheres which were used for computing contralateral and ipsilateral DAI and DTE distributions. Quality assurance for the outcomes of the image processing routines was conducted by three trainees, each with more than 2 years of experience (Hande Halilibrahimoğlu, Seda Keskin and Korhan Polat), inspected by an imaging scientist of 20+ years of experience (Alpay Özcan) and approved by a neuro–radiologist with 30+ years of experience (Alp Dinçer).

4.4 Data Preparation

DAI maps defined as functions of the DTEs (see Eqs. 1.3, 1.4, 1.5) and their distributions on the whole brain NAWM and each of the hemispheres were calculated with in–house developed MATLAB® software.

For each anisotropy index and eigenvalue respectively, the cohort's minimum and maximum values were used for defining a common histogram bin range. Using the corresponding bin range for each index, three histograms with 30, 60 and 90 equally spaced bins were computed for each patient.

The inter–patient mask volume variability was eliminated by normalizing each patient's histogram and thus converting it to a probability density function:

$$\bar{h}_k(l) = \frac{h_k(l)}{\sum_{i=1}^{m} h_k(i)} = \frac{h_k(l)}{N_k} \qquad \Rightarrow \qquad \sum_{i=1}^{m} \bar{h}_k(i) = 1 \tag{4.1}$$

where h_k and $\bar{h}_k$ respectively denote the distribution and the corresponding density function for the kth patient, l denotes the bin index, m denotes the total number of bins in the distribution and N_k denotes k^{th} patient's total number of mask pixels.

For using the normalized distributions as inputs to the MLAs, each normalized histogram was treated as a vector with entries equal to the bin counts. The difference between the contralateral and ipsilateral distribution functions of each patient, referred

to as hemisphere difference distributions, was calculated by subtracting normalized ipsilateral distributions from contralateral distributions. The cohort's set vectors for each index was mean–centered prior to running MLAs. Mean of each bin was calculated, creating an $1 \times$ n vector, and subtracted from each patient's density function:

$$\hat{h}_k(l) = \bar{h}_k(l) - \mu_{\bar{H}(l)} \tag{4.2}$$

where $\hat{h}_k(l)$ denotes mean–centered l^{th} bin of kth patient's distribution, $\bar{h}_k(l)$ denotes the lth bin of kth patient's density function and $\mu_{\bar{H}(l)}$ denotes the mean of the lth distribution bin calculated over the cohort. In addition, ADC, FA and RA maps were concatenated to yield "all DAI" distributions; λ_1, λ_2 and λ_3 distributions were concatenated to yield "all DTE" distributions. Feature selection methods were also applied to these concatenated distributions, and selected bins were used for classification.

4.5 Feature Selection and Extraction

Relevant characteristics of the distributions were identified with four feature selection and dimension reduction methods:

1. variance threshold [54],
2. sequential forward feature selection (SFFS) [55, 56, 57]
3. sequential backward feature selection (SBFS) [55, 56, 57]
4. singular value decomposition (SVD) [58, 59].

4.5.1 Variance Threshold

Features, i.e. count value at each bin, that remain constant within the cohort were removed by computing the variance of each bin's count values across the cohort. Then variance of each bin was scaled to [0 1] range with minmax scaling [60] for thresholding,

$$\hat{z} = \frac{z - z_{min}}{z_{max} - z_{min}} \tag{4.3}$$

where $\hat{z}$ denotes the scaled vector, z denotes the input vector, z_{max} and z_{min} denotes the minimum and maximum of the input vector. A heuristically chosen threshold value of 10^{-5} was used for removing features with cohort–variances below it [54].

4.5.2 Sequential Feature Selection

Sequential feature selection is a wrapper based feature selection technique which uses classifier performance to determine which feature to retain or remove. The selection criterion is selected as the minimum or maximum of a classifier performance metric, such as loss or accuracy, or a custom function of classifier performance. Sequential forward feature selection (SFFS) is initialized with an empty set and a feature satisfying the criterion is added on each iteration, until the criterion is no longer satisfied. Conversely, sequential backward feature selection (SBFS) is initialized with the full feature set and features are removed on each iteration, until no further removal criterion is reached [55, 57]. In this study, SFFS and SBFS was used to select the subset of most relevant distribution bins while considering the mutual interaction between the them [56, 57]. Features with minimum classification loss of a decision tree classifier, with leave–one–out cross–validation, were selected as the most relevant bins.

4.5.3 Singular Value Decomposition

Singular value decomposition (SVD) factors a rectangular matrix into two orthogonal matrices U, V and diagonal matrix Σ given by

$$A = U\Sigma V^T \tag{4.4}$$

The diagonal matrix Σ contains essential information of the original data matrix represented by the diagonal entries, which are the singular values [58, 59]. As the larger singular values are more significant than smaller ones, if we select the r largest singular values, then we can reconstruct a lower ranked data matrix with only the essential information, or we can extract r most significant basis vectors for the columns of A by:

$$Av_r = \sigma_r u_r \tag{4.5}$$

and reduce data dimensions. In this study, SVD was applied to anisotropy and eigenvalue distribution data matrices of whole-brain NAWM and hemisphere difference to extract basis vectors of the column space of the data.

SVD was computed for each data set using MATLAB®'s `svd` function and left–, right–singular vectors and singular values in descending order were obtained. Dimension reduction for each data set was realized by first computing the relative changes between consecutive singular values and then pruning the singular values after the 20% drop level with the corresponding singular vectors.

4.6 Distribution Parameters and Multimodal Gaussian Fitting

In order to compare the predictive performance of full distributions with standard distribution parameters, straightforward distribution features such as mean, standard deviation, median, kurtosis, skewness and 10th, 25th, 40th, 60th, 75th, 90th percentile values were calculated (see Appendix B for details). All parameters were scaled to [0 1] range with minmax scaling (Eq. 4.3), and mean–centered (Eq. 4.2) before classification.

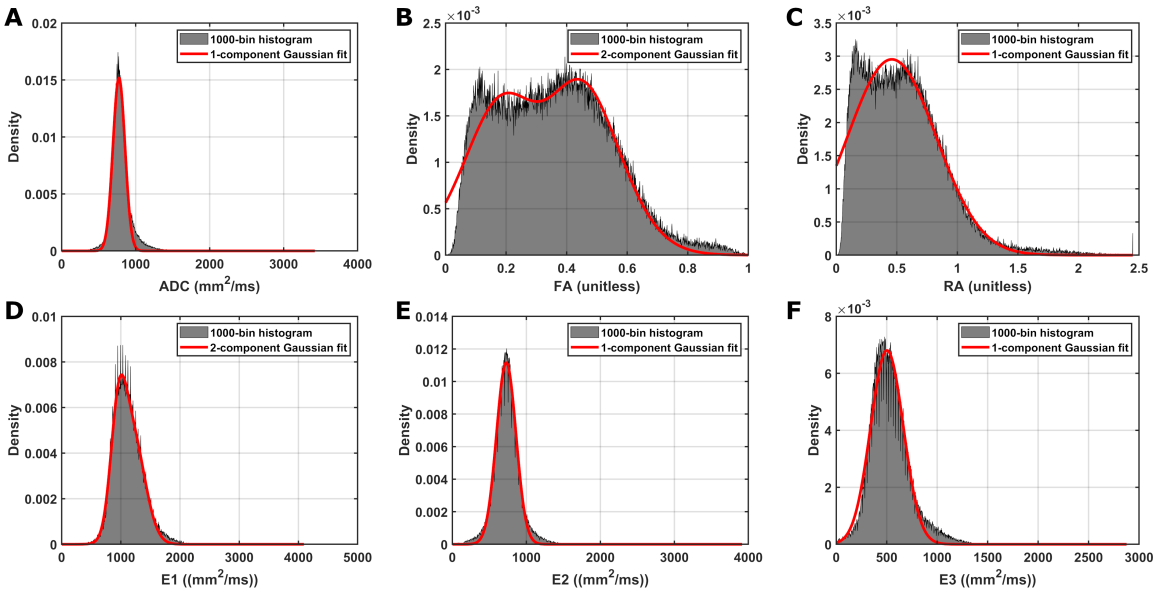

Figure 4.3 Whole brain NAWM (A) ADC, (B) FA, (C) RA, (D) λ_1, (E) λ_2, (F) λ_3 distributions and multimodal Gaussian fits of an example patient. Gray area: 1000-bin distribution. Red line: Multimodal Gaussian fit.

Distributions with multiple peaks and long–tails were observed in the data, similar to the reports in existing literature [16, 43, 45, 46, 48]. Accordingly, MGF was performed for summarizing distribution features such as peak locations and spread. Histograms were re–computed with 1000 bins for increasing sampling resolution and thereby improving the fitting process. Histograms were normalized to obtain probability density functions (see Section 4.4) and a Gaussian function is fitted to 1000–bin distribution of each patient:

$$y = \sum_{i=1}^{n} a_i \exp\Big[- \Big(\frac{x - b_i}{c_i} \Big)^2 \Big] \tag{4.6}$$

where n is the number of Gaussian components, a_i is the amplitude , b_i is the location or centroid, and c_i is the peak width of the ith component [61] (Figure 4.3). For an n–component Gaussian fit, starting values were initialized as the n highest points and n modes for amplitude and centroid, respectively. Width parameter was initialized as 100 for ADC and DTEs, and 0.1 for FA and RA. Following initialization, distributions of each patient was fitted with $n = 1...6$–component Gaussian functions with MATLAB® Curve Fitting Toolbox®'s non–linear least squares function. Non–linear least squares function aims to iteratively solve for coefficients a such that

$$\min_d \|F(d, x) - \hat{y}\|_2^2 = \min_i \sum_i (F(d, x_i) - \hat{y}_i)^2 \tag{4.7}$$

where $F(d, x)$ is a matrix–valued or vector–valued non–linear function which in this study is a Gaussian function, x is the input data, $\hat{y}$ is the observed data and d is the coefficients of non–linear function [62].

For each fit with n Gaussians, the root mean square error (RMSE) was calculated for each patient,

$$RMSE = \sqrt{\frac{\sum_{m=1}^{M} (y_m - \hat{y}_m)^2}{M}} \tag{4.8}$$

where M is the number of source distribution bins, $\hat{y}$ is the observed function value and y is the predicted or fitted function value [63].

The RMSE values were then averaged over the cohort for obtaining the mean root mean square error (mRMSE) at each n:

$$mRMSE = \frac{1}{K}\sum_{k=1}^{K} RMSE_n \tag{4.9}$$

where K is the number of patients, $RMSE_n$ is the RMSE of n–component Gaussian fit. For each anisotropy index and eigenvalue, the best number of Gaussians was determined by the multi–Gaussian fit with the lowest mRMSE value.

Coefficients of best fitting n Gaussians were extracted,mean-centered (See Equation 4.2) and used as features in classification. Furthermore, standard distribution parameters and MGF parameters of ADC, FA and RA maps were concatenated to create "all DAI" parameters; λ_1, λ_2 and λ_3 were concatenated to create "all DTE" parameters, which were then used for mutation prediction.

4.7 Dimensionality Comparison of MGF in mRMSE and SVD

The multi–Gaussian fit and SVD are two methods describing the set of basis vectors that would best represent the data. The dimensionality obtained from these two methods is used in determining dimensions of whole brain NAWM as well as contralateral and ipsilateral hemispheres' number of Gaussian components in MGF. To compare the performance of dimensions selected with mRMSE and SVD, number of best fitting Gaussian components for each DAI and DTE map were determined with mRMSE and SVD, then their parameters were used in molecular subgroup prediction.

Dimension selection with mRMSE was realized with method described in Section 4.6. For SVD dimensionality selection, 1000–bin DAI and DTE density functions were recalculated in the whole brain, contralateral and ipsilateral NAWM. SVD was

applied to these distributions, and relative change between singular values were calculated. Number of singular values below 20% relative change cut-off were selected as the number of Gaussians to be fitted (See Section 4.5.3 for details of SVD and cut-off).

4.8 Statistical Analysis and Machine Learning

4.8.1 Statistical Analysis

Statistical analysis was performed on whole brain NAWM and hemisphere difference DAI and DTE medians using MATLAB® Statistics and Machine Learning Toolbox® . DAI and DTE distributions were either multimodal, skewed or kurtotic, promoting the use of DAI and DTE medians instead of their means. DAI and DTE medians were compared with Kruskal–Wallis test, followed by post–hoc Dunn–Sidak test among IDH–TERT subgroups [64]. Dunn–Sidak correction was applied in post–hoc analysis, and $p < 0.0085$ determined statistical significance. Diffusion differences among IDH mutation and TERT mutation status were compared using Mann–Whitney U–test with $p < 0.05$ determining the statistical significance. Hemisphere difference DAI and DTE medians were calculated by subtracting ipsilateral NAWM means from contralateral NAWM means.

4.8.2 Machine Learning

Whole brain and hemisphere difference NAWM DAI and DTE distribution parameters, full distributions, features of full distributions and multimodal Gaussian sums were used to predict IDH–TERT subgroups, IDH and TERT mutations, using MLAs available in MATLAB® Statistics and Machine Learning Toolbox®. MLAs were run with the DAI and DTE parameters in whole brain NAWM and hemisphere difference, or contralateral and ipsilateral NAWM separately for MGF parameters for the following data representations:

- Distribution parameters
- Full distributions
- Variance thresholding applied to full distributions
- SFFS applied to full distributions
- SBFS applied to full distributions
- SVD applied to full distributions
- MGF, number of components selected with mRMSE
- MGF, number of components selected with SVD

In all, 912 classifications, with 24 MLAs for each run, were performed with each DAI and DTE map in whole brain NAWM and hemisphere difference for IDH–TERT subgroups, IDH and TERT mutation predictions. MLAs included the following algorithms: Gaussian naive bayes, kernel naive bayes, logistic regression, linear support vector machine (SVM), quadratic SVM, cubic SVM, fine Gaussian SVM, medium Gaussian SVM, coarse Gaussian SVM, linear discriminant, quadratic discriminant, coarse tree, fine tree, medium tree, fine k–nearest neighbor (kNN), medium kNN, cosine kNN, cubic kNN, coarse kNN, weighted kNN, AdaBoostM2–boosted trees, bagged trees, subspace discriminant, subspace kNN, RUS–boosted trees.

4.8.2.1 Decision Trees. A decision tree is a nonparametric hierarchical classifier, that does not make any assumptions on the data or label distribution [55]. Decision trees make a prediction by recursively splitting the data until an output is reached. Such recursive splits are made at decision nodes, where if–then functions split the data until a leaf node is reached. Decision boundaries are drawn at the leaf node, where similar inputs reside in the same decision region, thus localizing inputs with the same predicted labels in the same region. The value of the leaf node is the classification label in a classification problem. A decision tree's decision nodes can be expressed as

if–then rules to understand each decision, which makes decision tree an interpretable machine learning algorithm.

4.8.2.2 Support Vector Machines. SVM is a discriminant-based method that expresses class margins as a linear of sums of the influences of the subset of the training data, also called the support vectors. In SVM classification, a convex-optimization problem with a single optimum solution is solved [55] to maximize the margin. Kernel functions are used to map the input data to new space to find a linear solution in a complex space, which can be written as the sums of the influences of the support vectors, defined as the subset of training data that are close to class margin. A good kernel function maximizes class margins in its own space. Variants of SVMs use different kernel functions, such as linear, quadratic or Gaussian functions.

4.8.2.3 k-Nearest Neighbors. kNN algorithm is a nonparametic classification algorithms, which predicts the class of a new input as the class of its k nearest neighbors [55]. For a given test input, distance, such as Eucledian or Mahalanobis distance, of the test input with each of the data points is calculated and k nearest neighbors are identified. The class of the test input is assigned as the class of the majority of the k–nearest neighbors, determined by a simple vote. Without any weighting, each k–nearest neighbors' weights are equal, and class of the majority of neighbors are assigned to the test input. Usually, an odd number of k neighbors are selected to avoid ties in the majority voting. In the case of weighting, the vote of each neighbor is multiplied with a weight that either limits or increases its contribution to the vote.

4.8.2.4 Ensemble Methods. A single classifier or a single set of hyperparameters may not work well in a classification problem. In that case, ensemble learning, combining different classifiers or combining different hyperparameters of a single classifier, can improve classification accuracy [55]. Boosted trees, bagged trees, RUS boosted trees are examples of ensemble methods. Classifiers can be combined by voting; where

accuracy is determined as the average accuracy of all classifiers; as well as bagging or boosting. In bagging, each classifier is trained on a slightly different subset of training data and accuracies are combined by taking a vote. Boosting is done by training classifiers from the mistakes of other classifiers.

4.8.2.5 Performance Evaluation. Validation accuracy, sensitivity, specificity and precision, averaged over the executions and classes were calculated;

$$\text{Accuracy} = 1 - \frac{1}{g}\sum_{j=1}^{g} I\{\hat{y}_j \neq y_j\} \tag{4.10}$$

$$\text{Sensitivity} = \frac{1}{g}\sum_{j=1}^{g} \frac{\text{TP}_j}{\text{TP}_j + \text{FN}_j} \tag{4.11}$$

$$\text{Specificity} = \frac{1}{g}\sum_{j=1}^{g} \frac{\text{TN}_j}{\text{TN}_j + \text{FP}_j} \tag{4.12}$$

$$\text{Precision} = \frac{1}{g}\sum_{j=1}^{g} \frac{\text{TP}_j}{\text{TP}_j + \text{FP}_j} \tag{4.13}$$

where g denotes total number of classes; TP_j, TN_j, FP_j, FN_j denotes true positives, true negatives, false positives and false negatives for the jth class, respectively, and I denotes the indicator function which has a value of 1 if $\hat{y}_j = y_j$ and 0 otherwise [65]. These metrics were used to evaluate molecular subgroup predictions with a higher value in each metric indicating better performance. Due to large number of combinations tested, only the models with the highest validation accuracy is reported for each DAI and DTE. In case of ties in validation accuracy, the model with highest sensitivity was selected.

5. RESULTS

5.1 Statistical Analysis

Table 5.1
Comparison of whole brain NAWM and hemipshere difference medians IDH–TERT molecular subgroups with Kruskal–Wallis test. * *indicates* $p < 0.05$.

NAWM Coverage	Diffusion Map	p–value
Whole brain	ADC	0.2657
	FA	0.0010*
	RA	0.0010*
	λ_1	0.0343*
	λ_2	0.0244*
	λ_3	0.0102*
Hemisphere difference	ADC	0.1624
	FA	0.0001*
	RA	0.0001*
	λ_1	0.0056*
	λ_2	0.0736
	λ_3	0.0154*

Table 5.1 summarizes the results of the Kruskal–Wallis test for comparing whole brain NAWM and hemisphere difference diffusion anisotropy and eigenvalues in IDH–TERT subgroups. Figure 5.1 shows median values of whole brain NAWM and hemisphere difference diffusion anisotropy indices and eigenvalues, among IDH–TERT subgroups, IDH mutation and TERT mutation.

All whole brain NAWM eigenvalues, FA and RA were statistically significantly different in IDH–TERT subgroups ($p < 0.05$), whereas ADC showed no significant difference ($p = 0.2657$).

According to post-hoc Dunn–Sidak test, among IDH–TERT subgroups, whole

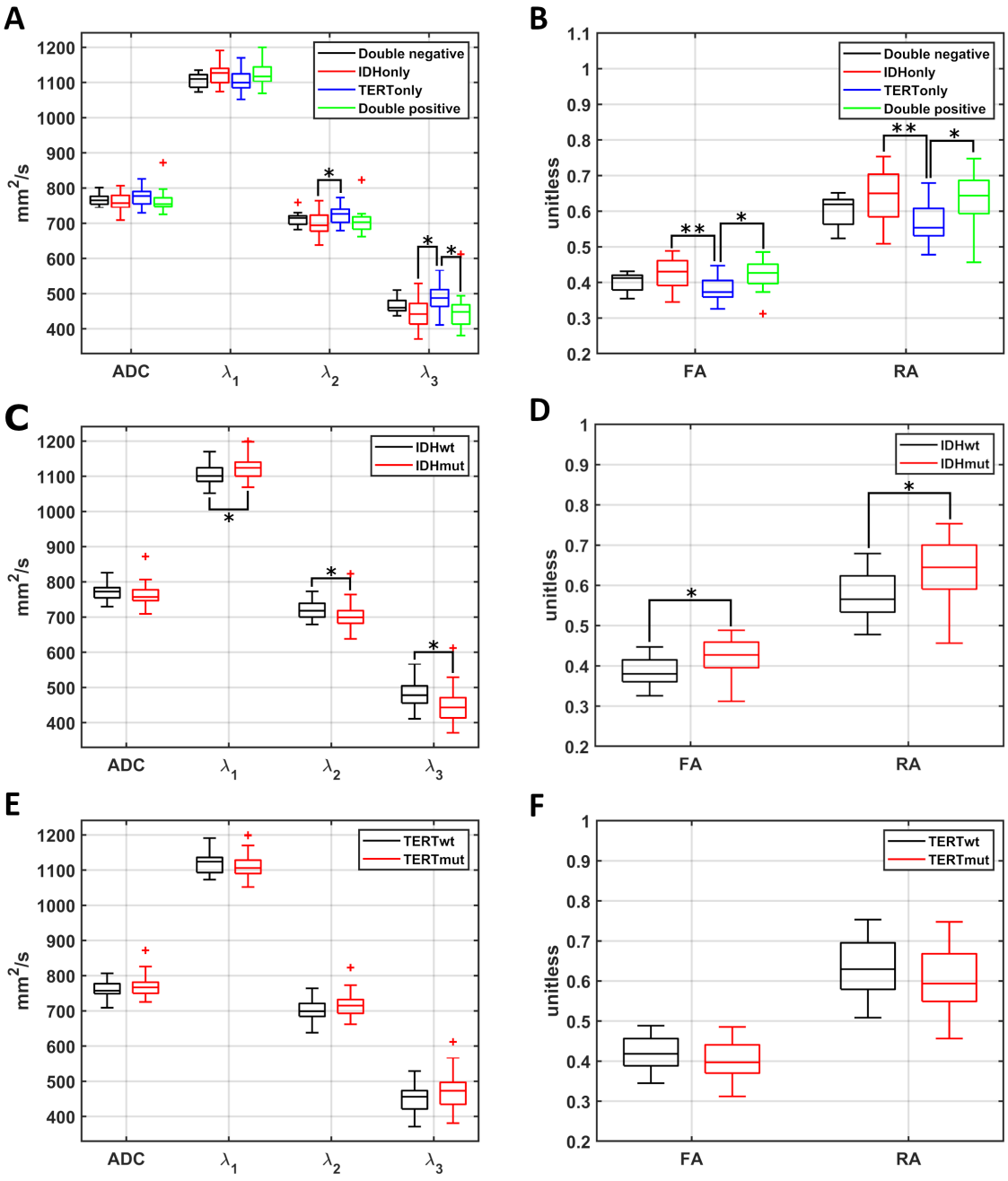

Figure 5.1 Boxplots of whole brain NAWM (A) ADC and DTE medians and (B) FA and RA medians grouped by IDH–TERT subgroups, (C) ADC and DTE medians and (D) FA and RA medians grouped by IDH mutation, (E) ADC and DTE medians and (F) FA and RA medians grouped by TERT mutation status. * indicate statistical significance < 0.05, $*$* indicate statistical significance < 0.0085 according to Dunn–Sidak correction for post-hoc analysis.

brain NAWM FA and RA were higher in IDHonly group than TERTonly ($p < 0.0085$), while showing a trend towards lower values in TERTonly patients compared to double positive ($p < 0.05$).

In whole brain NAWM eigenvalues, λ_2 and λ_3 showed a trend towards lower values in IDHonly patients compared to TERTonly ($p < 0.05$). Additionally, λ_3 tended to be higher in TERTonly group than double positive ($p < 0.05$). λ_1 did not demonstrate any statistically significant differences in post-hoc analysis.

Table 5.2
Comparison of whole brain NAWM hemipshere difference medians in IDH mutation status with Mann–Whitney U–test. * *indicates* $p < 0.05$.

NAWM Coverage	Diffusion Map	p–value
Whole brain	ADC	0.0580
	FA	0.0001*
	RA	0.0001*
	λ_1	0.0035*
	λ_2	0.0041*
	λ_3	0.0014*
Hemisphere difference	ADC	0.5391
	FA	< 0.0001*
	RA	< 0.0001*
	λ_1	0.0011*
	λ_2	0.7976
	λ_3	0.0457*

Table 5.2 and 5.3 show Mann-Whitney test results for the comparisons of whole brain NAWM and hemisphere difference diffusion anisotropy indices and eigenvalues in IDH mutation and TERT mutation status.

In IDH mutation status, IDHmut patients had higher whole brain NAWM FA, RA ($p = 0.0001$) and λ_1 ($p = 0.0035$), while IDHwt patients had higher λ_2 ($p = 0.0041$) and λ_3 ($p = 0.0014$). Whole brain NAWM ADC did not statistically significantly differ between IDHwt and IDHmut patients ($p = 0.0580$). In contrast to IDH mutation, no whole brain NAWM diffusion anisotropy index or eigenvalue demonstrated a statistically significant difference between TERTwt and TERTmut patients ($p > 0.05$).

Figure 5.2 shows median values of hemisphere difference diffusion anisotropy

Table 5.3
Comparison of whole brain NAWM hemipshere difference medians in TERT mutation status with Mann–Whitney U–test. * *indicates* $p < 0.05$

NAWM Coverage	Diffusion Map	p–value
Whole brain	ADC	0.4237
	FA	0.0647
	RA	0.0647
	λ_1	0.02661
	λ_2	0.1044
	λ_3	0.1614
Hemisphere difference	ADC	0.6253
	FA	0.0084*
	RA	0.0090*
	λ_1	0.2101
	λ_2	0.2585
	λ_3	0.0473*

indices and eigenvalues, among IDH–TERT subgroups, IDH mutation and TERT mutation.

All hemisphere difference eigenvalues as well as FA and RA were statistically significantly different among IDH–TERT subgroups ($p < 0.05$) (Table 5.1), whereas ADC did not show any statistically significant difference ($p = 0.1624$).

Post-hoc analysis demonstrated that among IDH–TERT subgroups, IDHonly and double positive patients had higher hemisphere difference FA and RA ($p < 0.0085$) compared to TERTonly patients. Hemisphere difference λ_1 trended towards lower values in double negative and TERTonly patients compared to IDHonly group ($p < 0.05$). Hemisphere difference ADC, λ_2 and λ_3 did not show any statistically significant differences in post-hoc analysis.

In IDH mutation status, IDHmut patients had higher hemisphere difference FA and and lower RA ($p < 0.0001$) (Table 5.2). Within hemisphere difference eigenvalues,

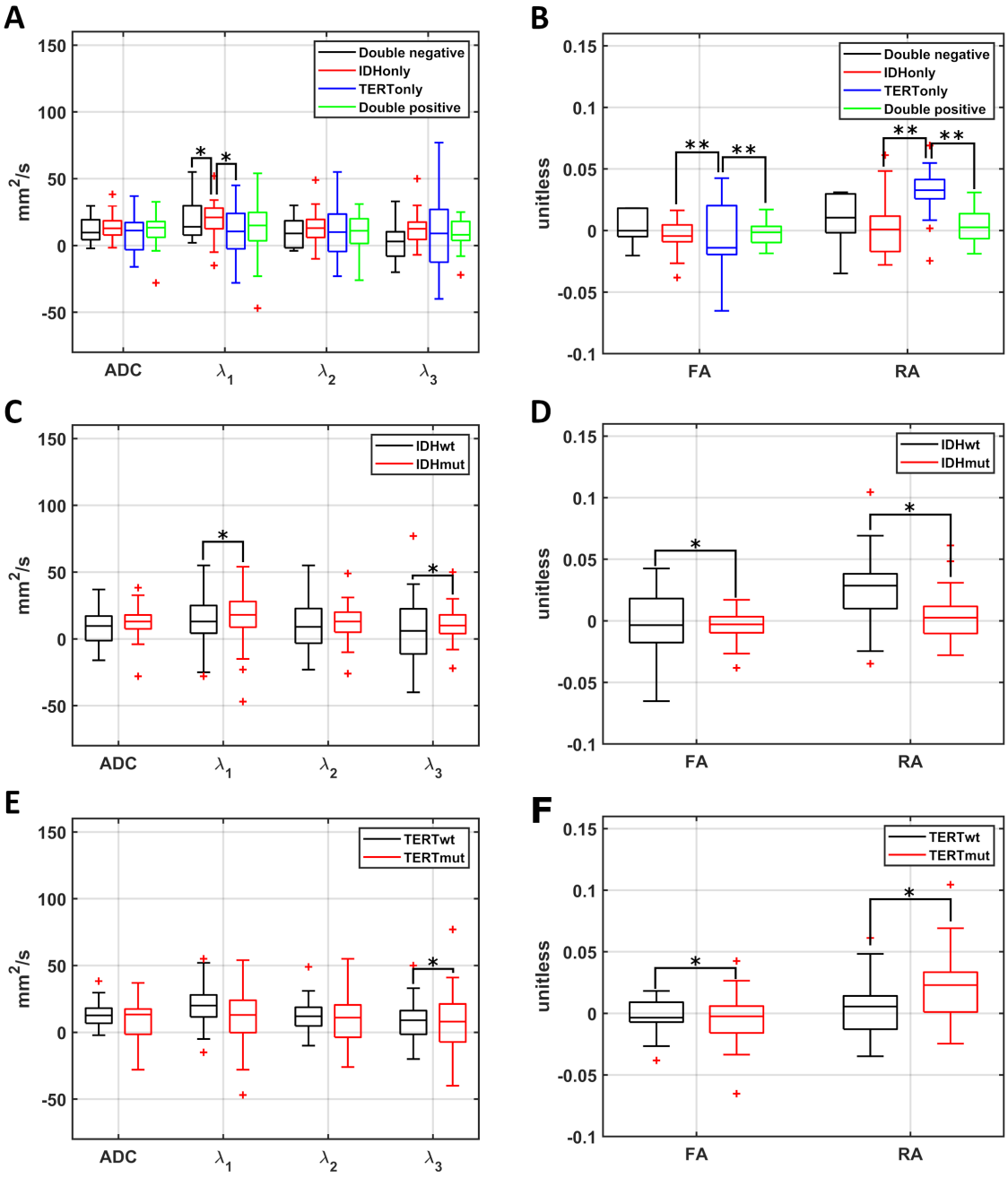

Figure 5.2 Boxplots of hemisphere difference (A) ADC and DTE medians and (B) FA and RA medians grouped by IDH–TERT subgroups, (C) ADC and DTE medians and (D) FA and RA medians grouped by IDH mutation, (E) ADC and DTE medians and (F) FA and RA medians grouped by TERT mutation status. * indicate statistical significance < 0.05, ** indicate statistical significance < 0.0085 according to Dunn–Sidak correction for post-hoc analysis.

λ_1 and λ_3 were higher in IDHmut patients in comparison to IDHwt ($p = 0.0011, p = 0.0457$, respectively). There was no statistically significant difference in hemipshere difference ADC ($p = 0.5391$) and λ_2 ($p = 0.7976$) between IDHmut and IDHwt groups.

TERTmut patients had higher hemisphere difference FA ($p = 0.0084$) and RA ($p = 0.0090$) than TERTwt, while TERTwt patients had higher hemisphere difference λ_3 ($p = 0.0473$). There were no statistically significant differences in hemisphere difference ADC ($p = 0.6253$), λ_1 ($p = 0.2101$) and λ_2 ($p = 0.2585$) of TERTmut and TERTwt patients.

5.2 MGF Dimensionality Selection

Table 5.4
mRMSE values of each Gaussian fit for each DAI and DTE. Boldfaced mRMSE values indicate the selected number of Gaussian sums.

		mRMSE Values ($\times 10^{-4}$)					
NAWM Hemisphere	**n =**	**1**	**2**	**3**	**4**	**5**	**6**
Whole brain	**ADC**	**3.17**	4.50	3.97	3.44	3.53	3.30
	FA	1.75	**1.70**	3.70	3.15	3.01	2.25
	RA	**1.98**	2.37	3.67	4.35	5.20	4.72
	$\boldsymbol{\lambda_1}$	3.20	**3.05**	5.88	8.89	9.33	7.73
	$\boldsymbol{\lambda_2}$	**2.64**	4.77	7.20	6.56	6.11	5.97
	$\boldsymbol{\lambda_3}$	**3.22**	6.36	6.40	6.97	6.76	6.42
Contralateral	**ADC**	**2.87**	3.90	3.64	3.25	3.20	3.13
	FA	**1.94**	1.94	3.69	2.94	2.88	2.44
	RA	**2.11**	2.49	3.16	3.19	4.31	3.86
	$\boldsymbol{\lambda_1}$	**3.19**	3.50	5.32	8.70	9.10	7.71
	$\boldsymbol{\lambda_2}$	**3.16**	6.16	6.87	6.89	6.32	6.11
	$\boldsymbol{\lambda_3}$	**4.04**	6.09	7.60	6.92	6.71	6.34
Ipsilateral	**ADC**	**3.46**	4.66	4.17	3.55	3.64	3.55
	FA	**2.28**	2.38	3.42	2.61	3.20	2.64
	RA	2.30	**2.25**	3.66	2.83	3.71	3.13
	$\boldsymbol{\lambda_1}$	3.51	**3.25**	6.65	8.43	8.65	7.74
	$\boldsymbol{\lambda_2}$	**4.32**	6.28	7.81	7.13	6.77	6.32
	$\boldsymbol{\lambda_3}$	**3.39**	6.12	6.91	6.99	6.55	6.25

Table 5.4 shows resulting mRMSE values of each diffusion map after MGF fitting with $n = 1...6$ Gaussian components. 2–component Gaussian was selected as the best

fit for whole brain FA and λ_1, while 1–component Gaussian was selected as the best fit for whole brain ADC, RA, λ_2 and λ_3. For all diffusion maps of the contralateral NAWM, 1–component Gaussian was the best fit. In ipsilateral NAWM, 2–component Gaussian was selected for ipsilateral RA and λ_1, and 1–component Gaussian was selected as the best fit for ADC, FA, λ_2 and λ_3.

Table 5.5
Number of selected Gaussian components with SVD and their corresponding mRMSE for each DAI and DTE.

	Number of Gaussians/mRMSE ($\times 10^{-4}$)		
	Whole brain NAWM	**Contralateral NAWM**	**Ipsilateral NAWM**
ADC	6/3.30	6/3.17	5/3.64
FA	5/3.01	5/2.88	5/3.20
RA	5/5.20	5/4.31	5/3.71
$\boldsymbol{\lambda_1}$	5/9.33	5/9.10	5/8.65
$\boldsymbol{\lambda_2}$	5/6.11	5/6.32	4/7.53
$\boldsymbol{\lambda_3}$	6/6.42	6/6.61	5/6.55

Table 5.5 shows the number of Gaussian components selected with SVD and their corresponding mRMSE values. SVD selected 6 Gaussians for whole brain and contralateral NAWM ADC and λ_3 distributions, and 5 Gaussians for FA, RA, λ_1 and λ_2. Furthermore, 4 Gaussians were selected for ipsilateral NAWM λ_2 distributions, and 5 Gaussians for ipsilateral ADC, FA, RA, λ_1 and λ_3.

5.3 Machine Learning Results

5.3.1 Comparison of Distribution Representations

Figure 5.3 demonstrates the validation accuracies of whole brain NAWM and hemisphere difference full distributions and distribution parameters; whole brain, contralateral and ipsilateral NAWM MGF parameters where components were selected with mRMSE.

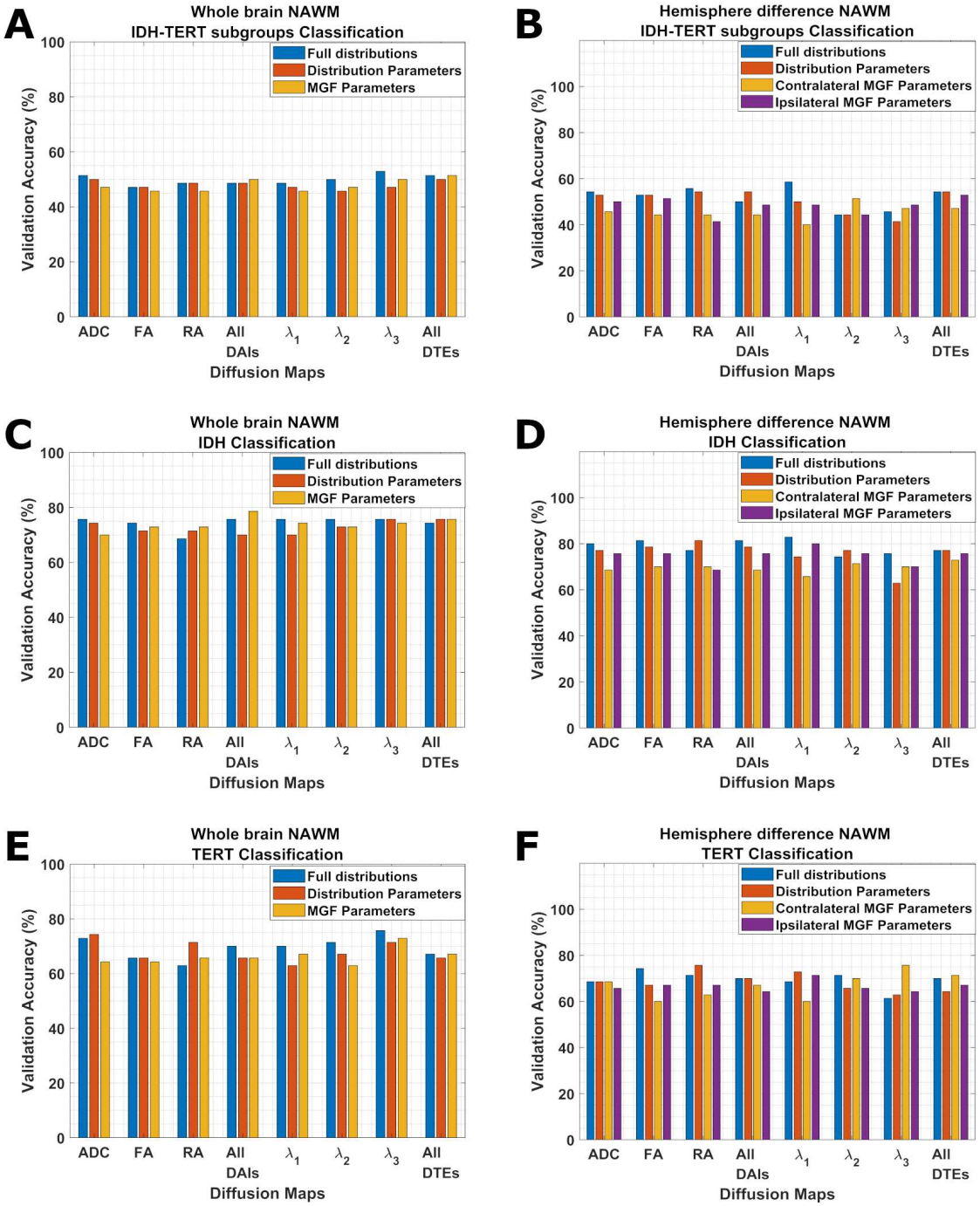

Figure 5.3 Validation accuracy comparison of whole brain NAWM and hemisphere difference full DAI and DTE distributions, distribtuion parameters and MGF parameters selected with mRMSE in (A–B) IDH–TERT subgroups, (C–D) IDH mutation, (E–F) TERT mutation classifications.MGF parameters were analyzed as contralateral and ipsilateral hemisphere for hemipshere difference analysis.

Table 5.6 summarizes the best performing whole brain NAWM and hemisphere difference diffusion distribution representations for IDH–TERT subgroups prediction.

Table 5.6
Classification results with the highest validation accuracy in IDH–TERT subgroup prediction using full distributions, distribution parameters and MGF parameters where components were selected with mRMSE. **Due to the class imbalance between the 4 classes of IDH–TERT subgroups, one of the class–wise precision calculations results in zero–division. This zero–division leads to NaN in averaged precision.*

NAWM Hemisphere	Diffusion Map	Dist. Type	MLA	Val. Acc. (%)	Sens. (%)	Spec. (%)	Prec. (%)
Whole Brain	ADC	Dist. params.	Medium kNN	50.0	41.3	82.1	38.9
	All DTEs		Cubic kNN	50.0	42.0	82.1	48.3
	ADC	90 bin	Cosine kNN	51.4	43.9	82.1	67.7
	λ_3	60 bin	Cubic kNN	52.9	44.3	83.2	39.5
	All DAIs	4–comp.	Cosine kNN	50.0	41.7	82.0	NaN*
	All DTEs	4–comp.	Subspace Discriminant	51.4	46.0	83.1	48.1
Hemisphere difference	All DAIs	Dist. params.	Kernel Naive Bayes	54.3	50.9	83.9	54.8
	All DTEs		Quadratic SVM	54.3	48.1	83.8	51.0
	RA	30 bin	Cubic kNN	55.7	48.3	84.3	49.1
	λ_1	30 bin	Kernel Naive Bayes	58.6	51.9	86.0	53.5
Contralateral	ADC	1–comp.	Subspace Discriminant	45.7	36.3	80.0	NaN*
	λ_2	1–comp.	Coarse Tree	51.4	41.7	82.4	NaN*
Ipsilateral	FA	1–comp.	Coarse Tree	51.4	46.0	82.2	52.7
	All DTEs	4–comp.	Fine Tree, Medium Tree	52.9	47.7	84.0	47.9

Among all distribution representations of whole brain NAWM, IDH–TERT mutation was best predicted by 60 bin λ_3 distributions with 52.9% validation accuracy in comparison to standard distribution and MGF parameters (Table 5.6). Similary, whole brain NAWM full distributions were the best predictors for ADC, λ_1, λ_2 and all DTEs (Figure 5.3). Full distributions and distribution parameters of FA, RA and all DAI maps had comparable classification performance, outperforming MGF parameters. 60 bin λ_3 distribution was the best hemisphere difference distribution representation for IDH–TERT classification with 58.6% validation accuracy (Table 5.6). If each DAI and DTE map were evaluated separately, full hemisphere difference distributions were the

best predictors for ADC and RA as well (Figure 5.3). In contrast, while FA, λ_2 and all full hemisphere difference DTE distributions predicted IDH–TERT subgroups with the same accuracy as the distribution parameters of these maps, distribution parameteres of all DAIs had increased predictive power than full distributions and MGF parameters. Lastly, contralateral NAWM MGF parameters were the representation with the highest validation accuracy for λ_2, and ipsilateral NAWM MGF parameters were for λ_3.

Table 5.7
Classification results with the highest validation accuracy in IDH mutation prediction using full distributions, distribution parameters and MGF parameters where components were selected with mRMSE.

NAWM Hemisphere	Diffusion Map	Dist. Type	MLA	Val. Acc. (%)	Sens. (%)	Spec. (%)	Prec. (%)
Whole brain	ADC	Dist.	Coarse Tree	74.3	74.5	74.5	73.9
	λ_3	params.	Coarse Tree	75.7	75.2	75.2	75.0
	All DAIs	90–bin	Medium kNN	75.7	74.7	74.7	75.0
	λ_1	60–bin	Cosine kNN	75.7	74.2	74.2	75.2
	All DAIs	4–comp.	Cosine kNN	78.6	79.2	79.2	78.3
	All DTEs	4–comp.	Medium kNN	75.7	75.7	75.7	75.2
Hemisphere difference	RA	Dist	Cosine kNN	81.4	80.6	80.6	81.0
	All DTEs	params	Cosine kNN	77.1	75.4	75.4	76.9
	FA	30–bin	Cubic kNN	81.4	80.1	80.1	81.3
	λ_1	30–bin	Bagged Trees	82.9	82.3	82.3	82.3
Contralateral	RA	1–comp.	Cubic kNN	70.0	70.9	70.9	70.3
	All DTEs	3–comp.	Cosine kNN	72.9	70.8	70.8	72.4
Ipsilateral	ADC	1–comp.	Cosine kNN	75.7	75.2	75.2	75.0
	All DAIs	4–comp.	Cosine kNN	75.7	75.2	75.2	75.0
	λ_1	2–comp.	Cubic kNN, Medium kNN	80.0	78.4	78.4	80.0

Table 5.7 summarizes the best performing whole brain NAWM and hemisphere difference diffusion distribution representations for IDH mutation prediction. Among all whole brain NAWM distributions, whole brain NAWM MGF parameters of all DAIs predicted IDH mutation with the highest validation accuracy of 78.6% (Table 5.7).

While whole brain NAWM MGF parameters were also the best representation for the RA map, full distributions were the best representations for ADC, FA, λ_1 and λ_2 (Figure 5.3). For whole brain NAWM λ_3 map, distribution parameters and full distributions predicted IDH mutation with the same accuracy. On the other hand, whole brain NAWM all DTE distribution parameters and MGF parameters also predicted IDH mutation with the same accuracy. 30 bin hemisphere difference λ_1 distribution parameters predicted IDH mutation with 82.9% validation accuracy and became the top performer among all hemisphere difference distribution representations (Table 5.7). Full distributions were also the best representation for ADC, FA, all DAIs and λ_2 (Figure 5.3). On the other hand, hemisphere difference distribution parameters were the predictors with the highest validation accuracy for RA. Furthermore, hemisphere difference distribution parameters and full distributions of all DTEs had comparable performance.

In TERT mutation prediction, whole brain NAWM 30 bin distributions had the highest validation accuracy with 75.7% among other whole brain NAWM distribution representations (Table 5.8). On an individual basis, full distributions were also the best distribution representation for ADC, all DAIs, λ_1 and λ_2, in TERT mutation classification (Figure 5.3). For FA maps, full distribution and distribution parameters had the same accuracy. A similar case was observed between all DTE distribution parameters and full distributions. Among hemipshere difference NAWM distribution representations, distribution parameters of RA and contralateral NAWM 1–component λ_3 MGF parameters predicted TERT mutation with 75.7% accuracy (Table 5.8). While, hemisphere difference distribution parameters were the best representation for λ_1, distribution parameters had the same predictive power as full distribution and contralateral MGF parameters for ADC and all DAIs (Figure 5.3). Furthermore, hemisphere difference full distribution was the best representation for FA and λ_2. Contralateral MGF parameters were the best predictors for all DTEs similar to λ_3.

5.3.1.1 Effect of NAWM Hemisphere. Figures 5.4, 5.5 and 5.6 compare the validation accuracies of whole brain NAWM and hemisphere difference full distribu-

Table 5.8
Classification results with the highest validation accuracy in TERT mutation prediction using full distributions, distribution parameters and MGF parameters where components were selected with mRMSE.

NAWM Hemisphere	Diffusion Map	Distribution Representation	MLA	Val. Acc. (%)	Sens. (%)	Spec. (%)	Prec. (%)
Whole brain	ADC	Distribution parameters	Medium kNN	74.3	73.9	73.9	74.5
	λ_3		Coarse Tree	71.4	72.0	72.0	72.6
	ADC	90–bin distribution	Cosine kNN	72.9	73.0	73.0	73.0
	λ_3	30–bin distribution	Medium kNN	75.7	75.4	75.4	75.8
	RA	1–component MGF	Cosine kNN	65.7	65.1	65.1	65.9
	λ_3	1–component MGF	Medium kNN	72.9	72.5	72.5	72.9
Hemisphere difference	RA	Distribution parameters	Coarse Tree	75.7	75.7	75.7	75.7
	λ_1		Fine Tree, Medium Tree	72.9	72.7	72.7	72.8
	FA	90–bin distribution	Logistic Regression	74.3	74.9	74.9	75.5
	λ_2	60–bin distribution	Fine Tree, Medium Tree	71.4	71.5	71.5	71.4
Contralateral	ADC	1–component MGF	Cubic kNN, Medium kNN	68.6	68.1	68.1	68.6
	λ_3	1–component MGF	Cosine kNN	75.7	75.6	75.6	75.7
Ipsilateral	RA	2–component MGF	Fine Tree, Medium Tree	67.1	67.3	67.3	67.2
	λ_1	2–component MGF	Fine Tree, Medium Tree	71.4	71.8	71.8	72.0

tions, distribution parameters and MGF parameters selected with mRMSE.

Focusing on full distributions, IDH–TERT subgroups were predicted the best with 30 bin hemisphere difference λ_3 distributions, among all full distributions (Table 5.6). If classification accuracies of whole brain NAWM and hemisphere difference distributions are compared for each diffusion map, hemisphere difference distributions had higher accuracy in ADC, FA, RA, all DAIs and all DTEs (Figure 5.4). In contrast, whole brain NAWM distributions of λ_2 and λ_3 were the best predictors for

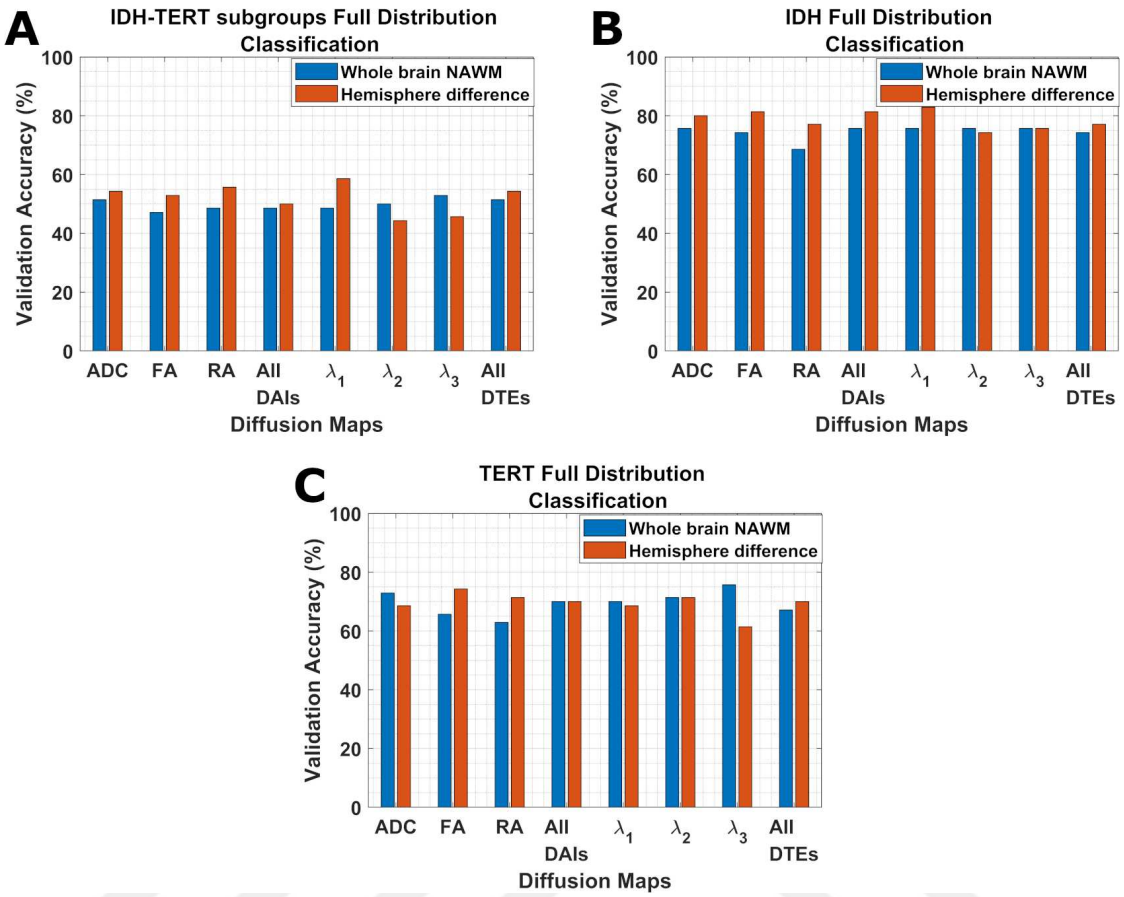

Figure 5.4 Validation accuracy comparison of the full whole brain NAWM and hemisphere difference DAI and DTE distributions for (A) IDH–TERT subgroups, (B) IDH mutation, and (C) TERT mutation classifications.

IDH–TERT subgroups for these maps. 30 bin hemisphere difference distribution of λ_1 predicted IDH mutation with 82.9% accuracy and became the top performer among all full distributions (Table 5.7). For individual DAI and DTE maps, hemisphere difference distributions had higher validation accuracy in comparison to their whole brain NAWM counterparts in ADC, FA, RA, all DAIs and all DTEs (Figure 5.4). While whole brain NAWM λ_1 distribution outperformed its hemisphere difference counterparts, performance of distributions from both hemispheric analysis were similar for λ_3. In contrast to IDH–TERT subgroups and IDH mutation predictions, TERT mutation was predicted the best by whole brain NAWM 30 bin λ_3 distribution (Table 5.8). Whole brain NAWM was the better predictor for ADC and λ_1 map in comparison to the corresponding hemisphere difference distribution (Figure 5.4). Whole brain NAWM and

hemisphere difference distributions of all DAIs and λ_1 had similar validation accuracies. Hemisphere difference distributions were the best predictors for FA, RA and all DTEs.

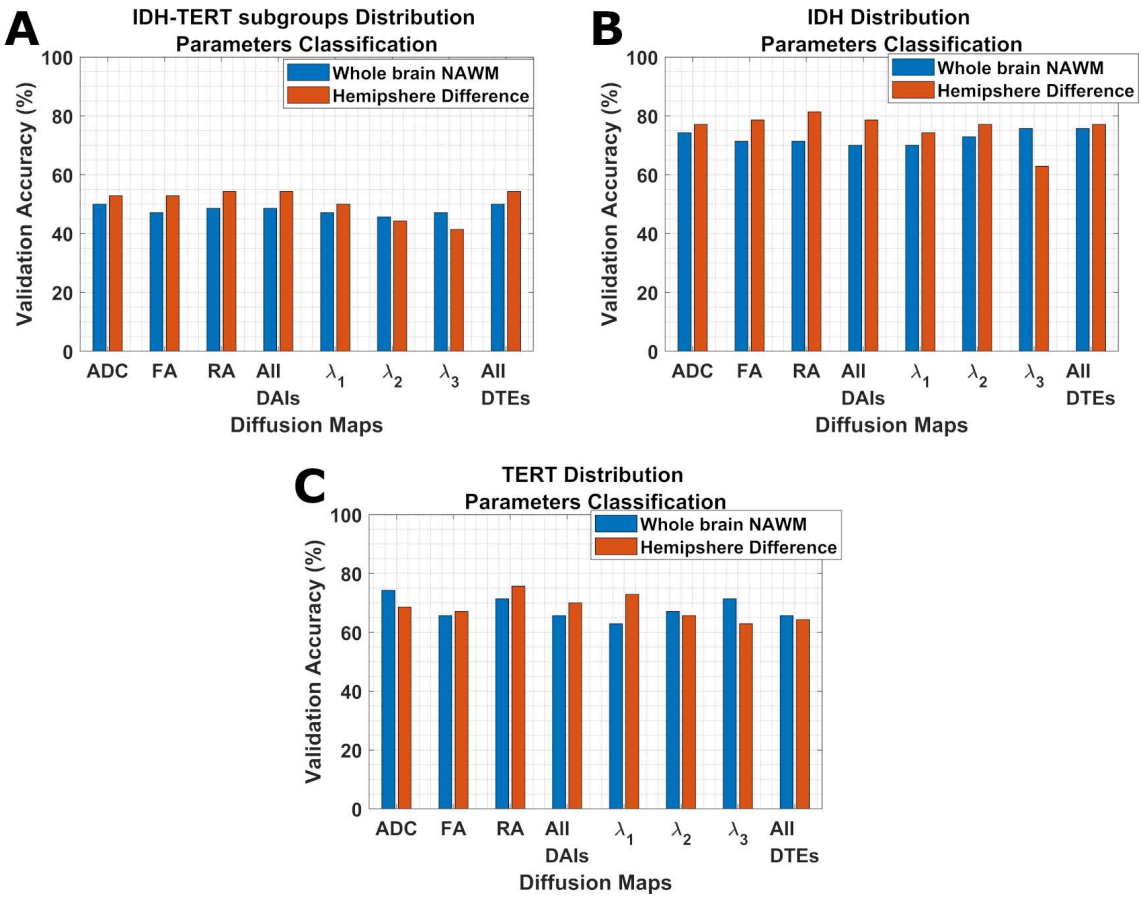

Figure 5.5 Validation accuracy comparison of the whole brain NAWM and hemisphere difference DAI and DTE distribution parameters for (A) IDH–TERT subgroups, (B) IDH mutation, and (C) TERT mutation classifications.

Among distribution parameters, IDH–TERT subgroups were best predicted by hemisphere difference distribution parameters of RA, all DAIs and all DTEs separately with 54.3% validation accuracy, and all DAIs had increased performance compared to RA in terms of sensitivity, specificity and precision (Table 5.6). Except for λ_2 and λ_3 maps, where whole brain NAWM distribution parameters had better predictive performance, hemisphere difference distribution parameters had better performance compared to their whole brain NAWM counterparts in ADC, FA and λ_1 (Figure 5.4). In IDH mutation prediction, hemisphere difference distributions of RA had the highest validation accuracy with 81.4% (Table 5.7). For each DAI and DTE, hemisphere

difference distributions of all diffusion maps had better classification accuracy in comparison to whole brain NAWM, except for λ_3 where whole brain NAWM distribution parameters resulted in higher accuracy (Figure 5.4). Similarly, hemisphere difference RA distribution parameters achieved the highest validation accuracy in TERT mutation prediction with 75.7% validation accuracy (Table 5.8). On an individual basis, whole brain NAWM distribution parameters had higher accuracy in ADC, λ_2, λ_3 and all DTEs, whereas hemisphere difference distribution parameters had higher accuracy in FA, all DAIs and RA (Figure 5.4).

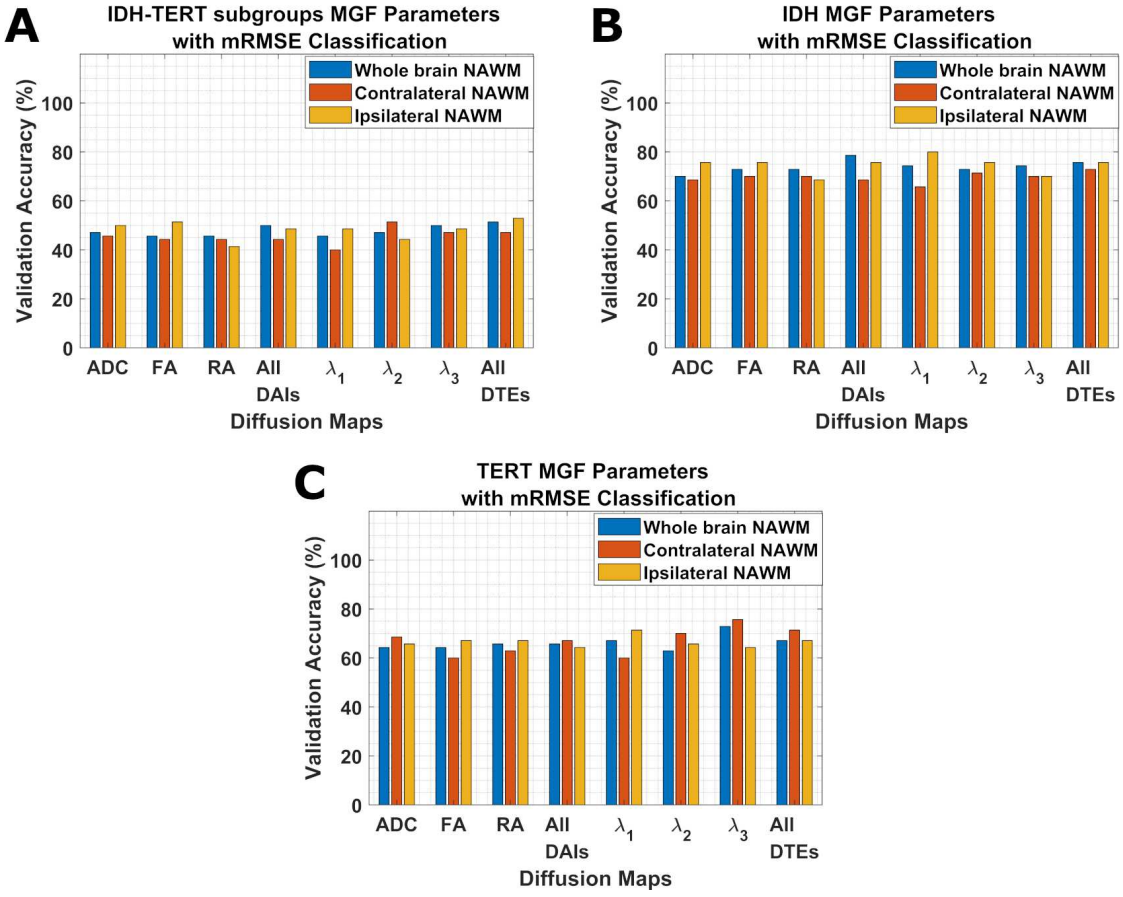

Figure 5.6 Validation accuracy comparison of the whole brain, contralateral, ipsilateral NAWM DAI and DTE MGF parameters for (A) IDH–TERT subgroups, (B) IDH mutation, and (C) TERT mutation classifications.

Among MGF parameters selected with mRMSE, IDH–TERT subgroups were predicted with the highest validation accuracy using ipsilateral NAWM 4–component MGF parameters of all DTEs (Table 5.6). Ipsilateral NAWM MGF parameters of

ADC, FA and λ_1 had higher validation accuracy in comparison to whole brain NAWM and contralateral NAWM MGF parameters of these maps. Furthermore, whole brain NAWM were the best predictors in comparison to other NAWM hemispheres in RA, all DAIs and λ_3 (Figure 5.6). In IDH mutation prediction, ipsilateral NAWM 2–component MGF parameters of λ_1 achieved the highest accuracy with 80.0% (Table 5.7). When each DAI and DTE is evaluated individually, ipsilateral NAWM MGF parameters were better predictors of IDH mutation for ADC, FA and λ_2, while ipsilateral NAWM MGF parameters of all DTEs had similar performance with whole brain NAWM MGF parameters of all DTEs (Figure 5.6). Whole brain NAWM MGF parameters had higher predictive value for RA, all DAIs and λ_3 maps in contrast to other NAWM hemispheres. In contrast to IDH–TERT subgroups and IDH predictions, TERT mutation was predicted the best by 1–component contralateral NAWM MGF parameters of λ_1 with 75.7% accuracy (Table 5.8). Considering each DAI and DTE map individually, contralateral NAWM MGF parameters were the best predictors for ADC, all DAIs, λ_2 and all DTEs(Figure 5.6). Furthermore, ipsilateral NAWM MGF parameters had higher accuracy in FA, RA and λ_1 maps.

5.3.2 Feature Selection Applied to Full Distributions

Table 5.9
Classification results with the highest validation accuracy in IDH–TERT subgroup prediction using full whole brain NAWM DAI and DTE distributions without and with feature selection.

Feature Selection	Diffusion Map	Number of Bins	MLA	Val. Acc. (%)	Sens. (%)	Spec. (%)	Prec. (%)
No Feature Selection	ADC	90	Cosine kNN	51.4	43.9	82.1	67.7
	λ_3	60	Cubic kNN	52.9	44.3	83.2	39.5
SBFS	All DAIs	90	Fine Tree, Medium Tree	78.6	77.0	92.5	78.1
	All DTEs	90	Fine Tree, Medium Tree	71.4	72.3	90.4	70.2

Figure 5.7 demonstrates the validation accuracy comparison of feature selection

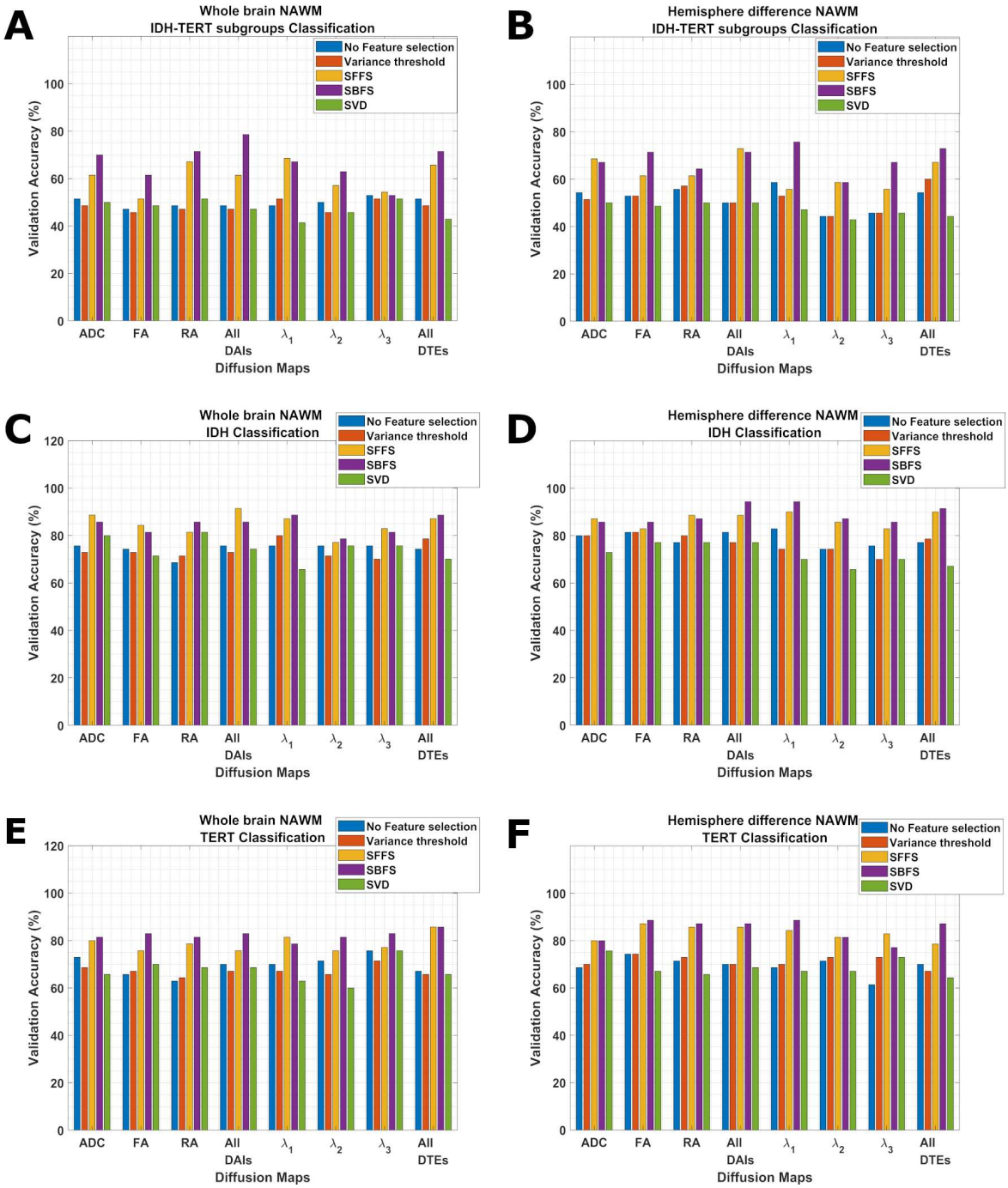

Figure 5.7 Validation accuracy comparison of feature selection methods applied to full whole brain NAWM and hemisphere difference DAI and DTE distributions in (A–B) IDH–TERT subgrops, (C–D) IDH mutation, (E–F) TERT mutation classifications.

methods applied to full distributions of whole brain NAWM and hemisphere difference for IDH–TERT subgroups, IDH and TERT mutation predictions.

Table 5.10
Classification results with the highest validation accuracy in IDH–TERT subgroup prediction using full hemisphere difference DAI and DTE distributions without and with feature selection.

Feature Selection	Diffusion Map	Number of Bins	MLA	Val. Acc. (%)	Sens. (%)	Spec. (%)	Prec. (%)
No Feature Selection	RA	30	Cubic kNN	55.7	48.3	84.3	49.1
	λ_1	30	Kernel Naive Bayes	58.6	51.9	86.0	53.5
SFFS	All DAIs	30	Boosted Trees	72.9	74.4	90.9	71.5
SFFS	λ_1	90	Fine Tree, Medium Tree	75.7	73.7	91.5	75.4

Tables 5.9 and 5.10 summarize the best performing whole brain NAWM DAI and DTE distributions without and with feature selection for IDH–TERT subgroups prediction.

For both whole brain NAWM and hemisphere difference distributions, SBFS was the feature selection that increased classification accuracy the most for most of the DAI and DTE maps (Figure 5.7) except for whole brain NAWM λ_1, hemisphere difference ADC and all DAIs with SFFS. Furthermore, hemisphere difference λ_2 distributions with SBFS and SFFS had similar prediction performance. Specifically, whole brain NAWM 90 bin distributions of all DAIs predicted IDH–TERT subgroups with 78.6% validation accuracy, while hemisphere difference 90 bin λ_1 distributions predicted with 75.7% validation accuracy (Table 5.10).

Tables 5.11 and 5.12 summarize the best performing whole brain NAWM DAI and DTE distributions without and with feature selection for IDH mutation prediction.

In IDH mutation prediction, SFFS applied all 90 bin DAI distributions achieved 91.4% validation accuracy (Table 5.11). SFFS also increased the validation accuracy the most for whole brain ADC, FA and λ_3, whereas SBFS was the top performing feature selection technique for RA, λ_1, λ_2 and all DTE maps (Figure 5.7). Using hemisphere difference distributions, SBFS applied 60 bin all DAIs and λ_1 distributions

Table 5.11
Classification results with the highest validation accuracy in IDH mutation prediction using full whole brain NAWM DAI and DTE distributions without and with feature selection.

Feature Selection	Diffusion Map	Number of Bins	MLA	Val. Acc. (%)	Sens. (%)	Spec. (%)	Prec. (%)
No Feature Selection	All DAIs	90	Medium kNN	75.7	74.7	74.7	75.0
	λ_1	60	Cosine kNN	75.7	74.2	74.2	75.2
SFFS	All DAIs	90	Fine Tree, Medium Tree	91.4	90.7	90.7	91.6
SBFS	All DTEs	60	Fine Tree, Medium Tree	88.6	87.7	87.7	88.6

Table 5.12
Classification results with the highest validation accuracy in IDH mutation prediction using full hemisphere difference DAI and DTE distributions without and with feature selection.

Feature Selection	Diffusion Map	Number of Bins	MLA	Val. Acc. (%)	Sens. (%)	Spec. (%)	Prec. (%)
No Feature Selection	FA	30	Cubic kNN	81.4	80.1	80.1	81.3
	λ_1	30	Bagged Trees	82.9	82.3	82.3	82.3
SBFS	All DAIs	60	Coarse Tree, Fine Tree, Medium Tree	94.3	93.6	93.6	94.7
	λ_1	60	Fine Tree, Medium Tree	94.3	93.6	93.6	94.7

separately predicted IDH mutation with 94.3% validation accuracy. SBFS improved the accuracy the most in λ_2, λ_3 and all DTEs as well. On the other hand, SFFS performed better for ADC, FA and RA hemisphere difference distributions.

Tables 5.13 and 5.14 summarize the best performing whole brain NAWM DAI and DTE distributions without and with feature selection for TERT mutation prediction.

Among all feature selection methods applied to whole brain NAWM distribu-

Table 5.13
Classification results with the highest validation accuracy in TERT mutation prediction using full whole brain NAWM DAI and DTE distributions without and with feature selection.

Feature Selection	Diffusion Map	Number of Bins	MLA	Val. Acc. (%)	Sens. (%)	Spec. (%)	Prec. (%)
No Feature Selection	ADC	90	Cosine kNN	72.9	73.0	73.0	73.0
	λ_3	30	Medium kNN	75.7	75.4	75.4	75.8
SBFS	FA	90	Fine Tree, Medium Tree	82.9	83.0	83.0	82.9
	All DTEs	90	Fine Tree, Medium Tree	85.7	85.8	85.8	85.7

Table 5.14
Classification results with the highest validation accuracy in TERT mutation prediction using full hemisphere difference DAI and DTE distributions without and with feature selection.

Feature Selection	Diffusion Map	Number of Bins	MLA	Val. Acc. (%)	Sens. (%)	Spec. (%)	Prec. (%)
No Feature Selection	FA	90	Logistic Regression	74.3	74.9	74.9	75.5
	λ_2	60	Fine Tree, Medium Tree	71.4	71.5	71.5	71.4
SBFS	FA	90	Fine Tree, Medium Tree	88.6	88.4	88.4	88.8
	λ_1	60	Fine Tree, Medium Tree	88.6	88.4	88.4	88.8

tions, SFFS and SBFS applied 90 bin distributions separately predicted TERT mutation with 85.7% validation accuracy, although they differed in sensitivity (Table 5.13). SBFS was the most successful method in increasing accuracy of whole brain NAWM full distributions for all DAI and DTE maps except for λ_2 for which SFFS was the most successful feature selection method (Figure 5.7). In hemisphere difference distributions, SBFS applied 90 bin FA and 60 bin λ_1 distribution predicted TERT mutation with the highest validation accuracy of 88.6% (Table 5.14). SFFS increased the accuracy of the hemisphere difference λ_3 distribution the most, whereas SBFS improved the accuracies

of hemisphere difference RA, all DAIs and all DTEs. On the other hand, SBFS and SFFS applied hemisphere difference ADC and λ_2 maps achieved similar performance.

5.3.3 Dimensionality Comparison in MGF

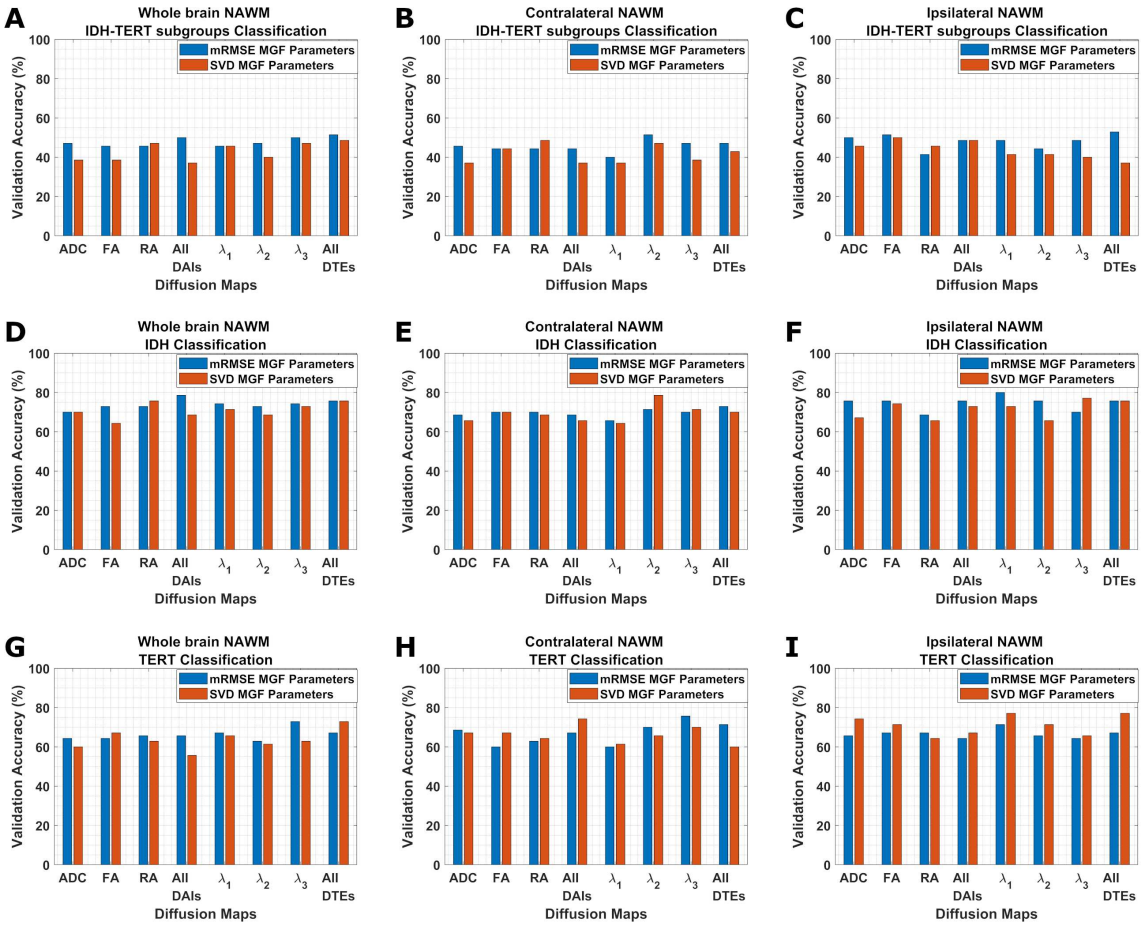

Figure 5.8 Validation accuracy comparison of DAI and DTE MGF parameters of whole brain, contralateral and ipsilateral NAWM whose components were selected with mRMSE and SVD in (A–C) IDH–TERT subgroups, (D–F) IDH mutation, (G–I) TERT mutation classifications.

Figure 5.8 demonstrates the validation accuracy comparison in dimensionality selection with mRMSE and SVD in MGF of whole brain, contralateral and ipsiateral NAWM for IDH–TERT subgroups, IDH and TERT mutation predictions.

Tables 5.15 and 5.16 show the best performing diffusion map of whole brain, contralateral and ipsilateral NAWM MGF parameters, where number of components

Table 5.15
Classification results with the highest validation accuracy in IDH–TERT subgroup prediction using MGF parameters of DAI and DTE distributions. Number of Gaussian components were selected with mRMSE. * *Due to the class imbalance between the 4 classes of IDH–TERT subgroups, one of the class–wise precision calculations results in zero–division. This zero–division leads to NaN in averaged precision.*

NAWM Coverage	Diffusion Map	Number of Gaussians	MLA	Val. Acc. (%)	Sens. (%)	Spec. (%)	Prec. (%)
Whole Brain	All DAIs	4	Cosine kNN	50.0	41.7	82.0	NaN*
	All DTEs	4	Subspace Discriminant	51.4	46.0	83.1	48.1
Contralateral	ADC	1	Subspace Discriminant	45.7	36.3	80.0	NaN*
	λ_2	1	Coarse Tree	51.4	41.7	82.4	NaN*
Ipsilateral	FA	1	Coarse Tree	51.4	46.0	82.2	52.7
	All DTEs	4	Fine Tree, Medium Tree	52.9	47.7	84.0	47.9

Table 5.16
Classification results with the highest validation accuracy in IDH–TERT subgroup prediction using MGF parameters of DAI and DTE distributions. Number of Gaussian components were selected with SVD using 20% relative change threshold. * *Due to the class imbalance between the 4 classes of IDH–TERT subgroups, one of the class–wise precision calculations results in zero–division. This zero–division leads to NaN in averaged precision.*

NAWM Coverage	Diffusion Map	Number of Gaussians	MLA	Val. Acc. (%)	Sens. (%)	Spec. (%)	Prec. (%)
Whole Brain	RA	5	Cosine kNN	47.1	40.3	81.0	46.7
	All DTEs	16	Cubic kNN	48.6	46.8	82.5	46.9
Contralateral	RA	5	Cosine kNN	48.6	40.1	81.4	NaN*
	λ_2	5	Medium kNN	47.1	41.2	81.4	35.9
Ipsilateral	FA	5	Linear SVM	50.0	44.6	82.2	52.1
	λ_1	5	Fine Tree, Medium Tree	41.4	40.1	80.1	39.3

were determined by mRMSE and SVD, for IDH–TERT subgroups prediction.

In IDH–TERT subgroups prediction, among whole brain NAWM MGF parameters, 4–component MGF selected with mRMSE achieved the highest validation accuracy with 51.4% (Table 5.15). For the remaining DAI and DTE maps, MGF components selected with mRMSE had higher accuracy than components selected with SVD for all maps except RA, which had higher accuracy with SVD, and λ_1, which had similar accuracy for mRMSE and SVD (Figure 5.8). In contralateral NAWM, 1–component λ_2 MGF parameters selected with mRMSE achieved the highest accuracy with 51.4% in comparison to SVD (Table 5.15). mRMSE selected components also outperformed SVD in all DAI and DTE maps, with the exception of FA, for which SVD performed better, and RA, where both dimensionality selection methods achieved similar accuracy (Figure 5.6). In ipsilateral hemisphere, mRMSE selected components of 4–component all DTEs achieved 52.9% validation accuracy (Table 5.15). Similarly, when DAI and DTE maps are evalauted individually, mRMSE selected components performed better than SVD for all DAI and DTE maps, except for RA where SVD outperformed mRMSE and all DAIs where both mRMSE and SVD predicted IDH–TERT subgroups with the same accuracies (Figure 5.8).

Table 5.17
Classification results with the highest validation accuracy in IDH mutation prediction using MGF parameters of DAI and DTE distributions. Number of Gaussian components were selected with mRMSE.

NAWM Coverage	Diffusion Map	Number of Gaussians	MLA	Val. Acc. (%)	Sens. (%)	Spec. (%)	Prec. (%)
Whole Brain	All DAIs	4	Cosine kNN	78.6	79.2	79.2	78.3
	All DTEs	4	Medium kNN	75.7	75.7	75.7	75.2
Contralateral	RA	1	Cubic kNN	70.0	70.9	70.9	70.3
	All DTEs	3	Cosine kNN	72.9	70.8	70.8	72.4
Ipsilateral	ADC	1	Cosine kNN	75.7	75.2	75.2	75.0
	All DAIs	4	Cosine kNN	75.7	75.2	75.2	75.0
	λ_1	2	Cubic kNN, Medium kNN	80.0	78.4	78.4	80.0

Tables 5.17 and 5.18 show the best performing diffusion map of whole brain, contralateral and ipsilateral NAWM MGF parameters, where number of components

Table 5.18
Classification results with the highest validation accuracy in IDH mutation prediction using MGF parameters of DAI and DTE distributions. Number of Gaussian components were selected with SVD using 20% relative change threshold.

NAWM Coverage	Diffusion Map	Number of Gaussians	MLA	Val. Acc. (%)	Sens. (%)	Spec. (%)	Prec. (%)
Whole Brain	RA	5	Cosine kNN	75.7	72.7	72.7	77.0
	All DTEs	16	Cosine kNN	75.7	74.2	74.2	75.2
Contralateral	FA	5	Medium kNN	70.0	66.8	66.8	70.0
	λ_2	5	Cubic kNN	78.6	77.2	77.2	78.2
Ipsilateral	FA	5	RUS Boosted Trees	74.3	74.0	74.0	73.6
	λ_3	5	Cosine kNN	77.1	73.9	73.9	79.4

were determined by mRMSE and SVD, for IDH mutation prediction.

Among whole brain NAWM MGF parameters, 4–component MGF parameters of all DAIs selected with mRMSE resulted in a 78.6% validation accuracy for IDH prediction (Table 5.17). mRMSE also performed better for FA, λ_1, λ_2 and λ_3 (Figure 5.8). For FA, SVD selected components achieved higher validation accuracy than mRMSE selected components. mRMSE and SVD selected components of ADC and all DTEs achieved similar accuracies. In contrast, in contralateral NAWM, 5–component MGF parameters of λ_2 selected with SVD achieved the highest validation accuracy with 78.6% (Table 5.18). For λ_3 SVD selected MGF parameters performed better than mRMSE, whereas both methods resulted in the same accuracy in IDH prediction (Figure 5.8). mRMSE outperformed SVD in ADC, RA, all DAIs, λ_1 and all DTEs.

Tables 5.19 and 5.20 show the best performing diffusion map of whole brain, contralateral and ipsilateral NAWM MGF parameters, where number of components were determined by mRMSE and SVD, for TERT mutation prediction.

In TERT mutation prediction with whole brain NAWM MGF parameters, 1–component MGF parameters of λ_3 selected with mRMSE and 16–component MGF

Table 5.19
Classification results with the highest validation accuracy in TERT mutation prediction using MGF parameters of DAI and DTE distributions. Number of Gaussian components were selected with mRMSE.

NAWM Coverage	Diffusion Map	Number of Gaussians	MLA	Val. Acc. (%)	Sens. (%)	Spec. (%)	Prec. (%)
Whole Brain	RA	1	Cosine kNN	65.7	65.1	65.1	65.9
	λ_3	1	Medium kNN	72.9	72.5	72.5	72.9
Contralateral	ADC	1	Cubic kNN, Medium kNN	68.6	68.1	68.1	68.6
	λ_3	1	Cosine kNN	75.7	75.6	75.6	75.7
Ipsilateral	RA	2	Fine Tree, Medium Tree	67.1	67.3	67.3	67.2
	λ_1	2	Fine Tree, Medium Tree	71.4	71.8	71.8	72.0

Table 5.20
Classification results with the highest validation accuracy in TERT mutation prediction using MGF parameters of DAI and DTE distributions. Number of Gaussian components were selected with SVD using 20% relative change threshold.

NAWM Coverage	Diffusion Map	Number of Gaussians	MLA	Val. Acc. (%)	Sens. (%)	Spec. (%)	Prec. (%)
Whole Brain	FA	5	Cubic kNN	67.1	67.8	67.8	68.5
	All DTEs	16	Coarse Tree	72.9	72.5	72.5	72.9
Contralateral	All DAIs	16	Coarse Tree	74.3	75.2	75.2	77.3
	λ_3	6	Coarse Tree	70.0	69.3	69.3	70.6
Ipsilateral	ADC	5	Coarse Tree	74.3	74.9	74.9	75.5
	All DTEs	14	Coarse Tree	77.1	77.9	77.9	79.3

parameters of all DTEs selected with SVD achieved the highest accuracy with 72.9% (Tables 5.19 and 5.20). When diffusion maps are evaluated individually, mRMSE selected components of ADC, all DAIs, λ_1 and λ_2 achived higher accuracies than SVD selected components, SVD selected components outperformed mRMSE selected components in FA (Figure 5.8). With contralateral NAWM MGF parameters, 1–component

λ_3 MGF parameters selected with mRMSE achieved the highest validation accuracy with 75.7% (Table 5.19). Among contralateral NAWM TERT prediction, mRMSE selected components resulted in increased accuracies for ADC, λ_2 and all DTEs. On the other hand SVD selected components had increased validation accuracy for FA, RA and λ_1. In ipsilateral NAWM, 5–component MGF parameters of λ_1 and 14–component MGF parameters of all DTEs selected with SVD achieved the highest accuracy in TERT prediction with 77.1%, although they differed in sensitivity (Table 5.20). SVD selected components also had higher validation accuracies in TERT predictions with ADC, FA, all DAIs and λ_2, whereas mRMSE selected components of RA had higher accuracies than RA MGF parameters selected with SVD (Figure 5.8).

6. DISCUSSION

In this study, the classification performances of whole brain and hemisphere difference diffusion anisotropy indices and eigenvalues' distributions of NAWM in predicting IDH–TERT subgroups, IDH and TERT mutations were analyzed. Full distributions as well as selected distribution bins and MGF parameters were used and the results were compared with those of standard histogram parameters. The results show that diffusion distributions can generally predict glioma molecular subgroups more accurately than standard distribution parameters. When whole brain NAWM and hemisphere difference distributions are compared, hemisphere difference distributions mostly achieved higher accuracy compared to their whole brain NAWM counterparts. Furthermore, using feature selection methods enhanced classification performance in all performance metrics used in this study. In addition, MGF component selection with mRMSE achieved higher accuracy compared component selection with SVD.

Differences of DAIs and DTE among IDH–TERT subgroups, IDH mutation and TERT mutation status were statistically compared. Among IDH–TERT subgroups, significant differences were detected among IDHonly and TERTonly subgroups with whole brain NAWM FA and RA. Hemisphere difference FA and RA also showed significant differences for the same subgroup pair and TERTonly and double positive groups. For the TERT mutation, no significant differences were found by whole brain NAWM DAIs and DTEs, however hemisphere difference FA and RA were higher, and λ_3 was lower in TERTmut patients than TERTwt. However, to the best of our knowledge, there are not any studies statistically comparing diffusion distributions between different TERT mutations or IDH–TERT subgroups. In IDH mutation, IDHmut patients have higher FA, RA, λ_1 and lower λ_2 and λ_3 compared to IDHwt. However, there was no significant difference in ADC. Higher FA and lower λ_2 and λ_3 agree with results of Jütten et al. [40], yet differ in ADC and λ_1. Lastly, hemisphere difference FA and RA were found to be lower, and hemisphere difference λ_1 and λ_3 were found to be higher in IDHmut patients in comparison to IDHwt. In this study, medians of diffu-

sion parameters were compared due to high skew, kurtosis or multi-modality of DAIs and DTEs. In contrast, mean values were used in the statistical analysis of Jütten et al. study, which might be the reason behind the disagreement in the findings for ADC and λ_1. Although nonparametric statistical tests have lower statistical power [64], such selection was made after checking for normality assumptions of parametric tests.

Classification performance of full distributions with standard distribution parameters and MGF-derived parameters of mRMSE, in whole brain and hemisphere difference NAWM were compared. MGF parameters of mRMSE were analyzed as contralateral and ipsialteral NAWM for hemisphere difference analysis, because different number of Gaussian components were selected by mRMSE for RA and λ_1 maps (Table 5.4). Our results confirm that full distributions are generally better predictors for glioma molecular subgroups than standard distribution parameters or multi–Gaussian fit parameters, in all NAWM hemipsheres and for all molecular subgroups labels, with some exceptions in IDH–TERT subgroups, IDH and TERT mutation (Figure 5.3). Although the findings agree with of Tozer et al. [15] who found raw tumor ADC histograms to be bettter predictors than histogram parameter for low-grade glioma subtypes, some DAIs and DTEs can better represent tumor effects in the NAWM caused by variations in IDH and TERT mutations with "simpler" distribution representations. Overall, this might suggest that while some diffusion parameters can be represented with summary statistics, others may need more complex representations such as MGF or full distributions.

Generally, hemisphere difference distribution representations had higher validation accuracies (Figures 5.4 and 5.5) in comparison to whole brain NAWM data. Exceptions to this observation was identified for eigenvalues and ADC data. MGF fit parameters of contralateral and ipsilateral NAWM had comparable to or better classification performance than whole brain NAWM distribution parameters. Of all full DAI and DTE distributions, hemisphere difference distributions had increased classification performance than most whole brain NAWM distributions, which might indicate the ability of hemisphere difference distributions' to capture DAI and DTE changes in NAWM caused by IDH and/or TERT mutations. Among contralateral and ipsilateral

NAWM MGF parameters, ipsilateral NAWM MGF parameteres had higher accuracy compared to contralateral NAWM except for contralateral NAWM λ_2 in IDH–TERT subgroup classification and ADC and λ_3 in TERT classification (Figure 5.6). This might suggest that TERT mutation may have more increased effects on contralateral NAWM MGF parameters, although this requires further investigation. Although distal changes have only been studied for different glioma grades only [32, 33], presence and prognosis of IDH and TERT mutated tumors have been linked to glioma grade [4, 11, 12, 13]. Varying IDH and TERT mutations might have caused varying magnitudes of change, with more pronounced diffusion changes in the ipsilateral NAWM. As a consequence, hemisphere difference distributions might be defined with different functions according to mutation status.

To use only the most informative subset of distribution bin columns, variance threshold, SFFS, SBFS and SVD were used. Among all feature selection and extraction methods, SFFS and SBFS selected features had the highest accuracy in all molecular subgroup predictions (Figure 5.7). These methods increased IDH–TERT prediction to 70% range and predicted IDH mutation with more than 90% accuracy and TERT mutation with more than 85% accuracy. In all predictions with SFFS and SBFS features, variants of decision trees were used to predict molecular subgroup labels, which might have an effect on increased accuracies. This confirms the observation that classifier used during feature selection process prepares the features for a specific MLA, which was a decision tree in this study [66].

To select a global number of Gaussians to fit to each diffusion map, 2 different methods, mRMSE and SVD, were used. mRMSE was calculated as the mean RMSE of each patient's fit. SVD was used to find the number of basis vectors that best defines the 1000–bin distribution, which was then selected as the number of Gaussians that models the full distribution. The results show that MGF parameters selected with mRMSE performed better or as well as MGF parameters selected with SVD in glioma subgroup prediction, although with some exceptions. For all diffusion maps SVD selected more Gaussian components than mRMSE in all maps. Classifications where SVD selected MGF components achieved higher accuracies than mRMSE, for

instance TERT prediction from ipsilateral NAWM, suggest the underlying data requires more complex Gaussians to predict genetic mutation, even though more components does not necessarily mean a better fit.

IDH–TERT subgroups prediction had the lowest classification performance irrespective of the features or feature selection method. This may be attributed to the effect of class imbalance in IDH–TERT subgroups. MLAs does not perform well under class imbalance because they learn examples of the majortiy class more than they learn the examples of the minority class. Inevitably, this results in high class-wise prediction accuracy for the majority class and low or zero accuracy for the minority class. Random undersampling (RUS) boosted trees are known for their robustness to imbalanced data, because this algorithm undersamples the majority class to balance class distributions before classification [67]. However, in this study, RUS boosted trees achieved the highest accuracy only in one of the classifications. Maps with highest validation accuracies generally used decision trees or kNN variants. This may be due to small size of the minority class, which causes underfitting during training (Figure 4.1). In future studies, oversampling methods, such as SMOTE [68] or A–SUWO [69] can be used to create a more uniform label distribution thus, increasing prediction performance.

Statistical analysis is a tool to draw inferences from sample data, where MLAs aim to recognize patterns and predict an outcome variable. As the number of variables increases, statistical model and analysis becomes more complex, and ML becomes a useful tools [70]. In this study, MLAs predicted mutations with diffusion maps that showed no statistical significance, for which ADC maps are examples. Statistical analysis was performed with one variable, the median values, yet the data were represented in a more complex manner, with full distributions and MGF parameters, in classification. This complexity may have been a factor that allowed maps that did not show any statistical signifcance to achieve the highest validation accuracy among all distribution parameters.

There are some limitations of this study. First of all, an in–house developed program was used to register NAWM masks from anatomical space to DTI space,

in order to correct for distortions caused by other registration tools. However, this program may not be able to delineate all NAWM areas as there were excluded islands belonging to NAWM tissue. Despite excluding some NAWM, masks registered with this program did not include any non–NAWM tissue. Second, cohort size decreased from 170 to 70 patients due to lack of imaging and genetic data in some patients, which is something expected in clinical data. In a clinical setting, physicians may not be able to perform genetic analysis due to time constraints imposed by the medical condition. Furthermore, imaging studies may have been cut short due complications related to tumor, resulting in certain missing imaging modalities.

In the future work, further studies are planned on a larger cohort to verify the success of DAI and DTE distributions in predicting IDH and TERT mutations in glioma patients. Furthermore, with MGF, instead of fitting a certain number of Gaussians to each diffusion map, number of fits of each patient will be studied and tested for mutation prediction.

7. CONCLUSION

In conclusion, this study demonstrated that more complicated data representations, namely full distributions and MGF parameters, may be more successful in predicting glioma genotype from NAWM DAIs and DTEs compared to standard summary statistics. Specifically , full diffusion distributions generally had increased predictive power compared to standard summary statistics and MGF parameters. Distal differences were investigated by testing distributions of whole brain NAWM and hemipshere difference. The results showed that hemisphere difference distributions generally predicted molecular subgroups with higher accuracy compared to whole brain NAWM distributions. In MGF parameters, data from ipsilateral NAWM mostly predicted IDH–TERT subgroups better than data from contralateral NAWM. Success of contralateral NAWM MGF data in TERT prediction suggests more investigation into the microstructural effects of TERT in the contralateral NAWM. Furthermore, using sequential feature selection significantly increased the classification accuracy and performance for all molecular subgroups included in this study. Considering the highly infiltrative and heterogenous behavior of gliomas, DAI and DTE information with varying complexities from NAWM provides a wider perspective and notable features for glioma molecular subgroup prediction.

8. List of publications produced from the thesis

1. Predicting Glioma Genotype Using n-Component Gaussian Distributions of Diffusion Anisotropy Distributions of Normal-Appearing White Matter, H. Halilibrahimoğlu, K. Polat, S. Keskin, K. Özduman, C. Yakıcıer, A. Erşen Danyeli, M. N. Pamir, A. Dinçer, E. Öztürk–Işık, A. Özcan, *European Society for Magnetic Resonance in Medicine and Biology, ESMRMB,* 2021 38th *Annual Scientific Meeting*, October 7–9, 2021

APPENDIX A. NAWM Mask Registration

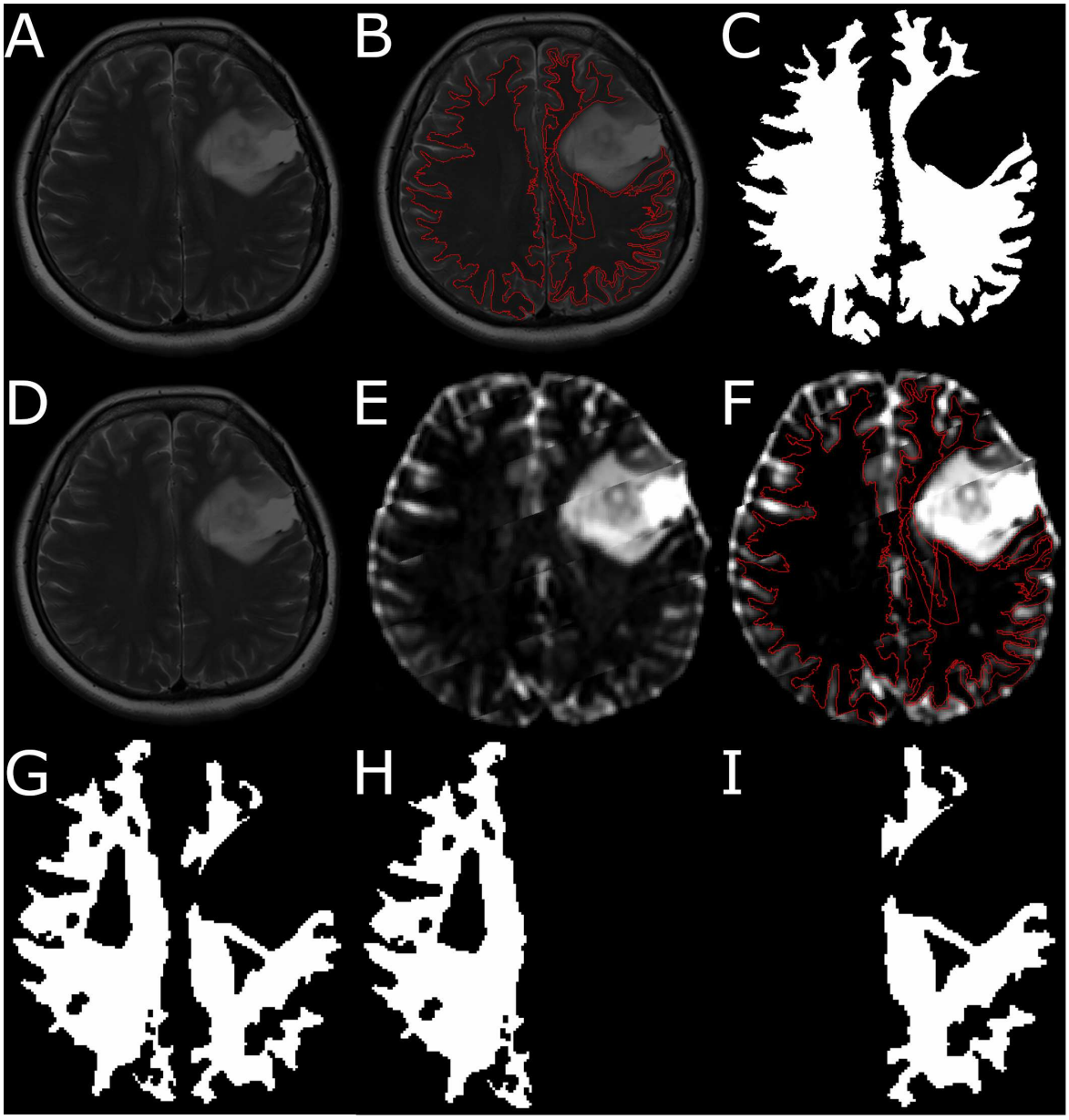

Figure A.1 Detailed steps of NAWM mask registration using in–house MATLAB® software. (A) T_2W image, (B) NAWM mask delineated in T_2W image space and (C) segmetation mask, (D) T_2W image, (E) B_0 map registered to T_2W imge sapce using FSL, (F) overlay of NAWM mask in T_2W image space on $B_0 \rightarrow T_2W$ image, (G–I) whole brain, left and right hemisphere NAWM masks registered to B_0 image space using in–house developed MATLAB® software.

APPENDIX B. Definitions of Distribution Parameters

In a sample with n elements, where x_i denotes the ith element [65, 71]:

B.1 Mean

$$\bar{x} = \frac{1}{n}\sum_{i=1}^{n} x_i \tag{B.1}$$

B.2 Standard Deviation

$$stdev = \sqrt{\frac{\sum_{i=1}^{n}(x_i - \bar{x})^2}{n-1}} \tag{B.2}$$

B.3 Median

If n is odd, median is calculated as the $\left(\frac{n+1}{2}\right)^{\text{th}}$ largest observation. If n is even, median is calculated as the mean of $\left(\frac{n}{2}\right)^{th}$ and $\left(\frac{n}{2}+1\right)^{\text{th}}$ observations.

B.4 Skewness

$$s = \frac{E(x-\bar{x})^3}{stdev^3} \tag{B.3}$$

where E denotes the expected value.

B.5 Kurtosis

$$k = \frac{E(x - \bar{x})^4}{stdev^4} \tag{B.4}$$

where E denotes the expected value.

B.6 p^{th} Percentile

p^{th} percentile point is defined as the $(k+1)^{\text{th}}$ largest elements of $\frac{np}{100}$ is not an integer, where k is the largest integer such that $k < \frac{np}{100}$. If $\frac{np}{100}$ is an integer, the pth percentile is defined as the mean of $\frac{np}{100}{}^{\text{th}}$ and $\left(\frac{np}{100}+1\right)^{\text{th}}$ elements.

REFERENCES

1. Ostrom, Q. T., N. Patil, G. Cioffi, K. Waite, C. Kruchko, and J. S. Barnholtz-Sloan, "CBTRUS statistical report: Primary brain and other central nervous system tumors diagnosed in the United States in 2013–2017," *Neuro-Oncology*, Vol. 22, pp. iv1–iv96, 10 2020.

2. Moton, S., M. Elbanan, P. O. Zinn, and R. R. Colen, "Imaging genomics of glioblastoma: Biology, biomarkers, and breakthroughs," *Topics in Magnetic Resonance Imaging*, Vol. 24, no. 3, pp. 155–163, 2015.

3. Louis, D. N., H. Ohgaki, O. D. Wiestler, W. K. Cavenee, P. C. Burger, A. Jouvet, B. W. Scheithauer, and P. Kleihues, "The 2007 who classification of tumours of the central nervous system," *Acta Neuropathologica*, Vol. 114, no. 2, pp. 97–109, 2007.

4. Eckel-Passow, J. E., D. H. Lachance, A. M. Molinaro, K. M. Walsh, P. A. Decker, H. Sicotte, M. Pekmezci, T. Rice, M. L. Kosel, I. V. Smirnov, G. Sarkar, A. A. Caron, T. M. Kollmeyer, C. E. Praska, A. R. Chada, C. Halder, H. M. Hansen, L. S. McCoy, P. M. Bracci, R. Marshall, S. Zheng, G. F. Reis, A. R. Pico, B. P. O'Neill, J. C. Buckner, C. Giannini, J. T. Huse, A. Perry, T. Tihan, M. S. Berger, S. M. Chang, M. D. Prados, J. Wiemels, J. K. Wiencke, M. R. Wrensch, and R. B. Jenkins, "Glioma groups based on 1p/19q, IDH, and TERT promoter mutations in tumors," *New England Journal of Medicine*, Vol. 372, no. 26, pp. 2499–2508, 2015. PMID: 26061753.

5. Louis, D. N., A. Perry, G. Reifenberger, A. von Deimling, D. Figarella-Branger, W. K. Cavenee, H. Ohgaki, O. D. Wiestler, P. Kleihues, and D. W. Ellison, "The 2016 world health organization classification of tumors of the central nervous system: a summary," *Acta Neuropathol*, Vol. 131, no. 6, pp. 803–20, 2016.

6. Parsons, D. W., S. Jones, X. Zhang, J. C.-H. Lin, R. J. Leary, P. Angenendt, P. Mankoo, H. Carter, I.-M. Siu, G. L. Gallia, A. Olivi, R. McLendon, B. A. Rasheed, S. Keir, T. Nikolskaya, Y. Nikolsky, D. A. Busam, H. Tekleab, L. A. Diaz, J. Hartigan, D. R. Smith, R. L. Strausberg, S. K. N. Marie, S. M. O. Shinjo, H. Yan, G. J. Riggins, D. D. Bigner, R. Karchin, N. Papadopoulos, G. Parmigiani, B. Vogelstein, V. E. Velculescu, and K. W. Kinzler, "An integrated genomic analysis of human glioblastoma multiforme," *Science*, Vol. 321, no. 5897, pp. 1807–1812, 2008.

7. Yang, H., D. Ye, K.-L. Guan, and Y. Xiong, "Idh1 and idh2 mutations in tumorigenesis: Mechanistic insights and clinical perspectives," *Clinical Cancer Research*, Vol. 18, no. 20, pp. 5562–5571, 2012.

8. Turkalp, Z., J. Karamchandani, and S. Das, "IDH mutation in glioma: New insights and promises for the future," *JAMA Neurology*, Vol. 71, pp. 1319–1325, 10 2014.

9. Colebatch, A. J., A. Dobrovic, and W. A. Cooper, "TERT gene: its function and dysregulation in cancer," *Journal of Clinical Pathology*, Vol. 72, no. 4, pp. 281–284, 2019.

10. Vinagre, J., V. Pinto, R. Celestino, M. Reis, H. Pópulo, P. Boaventura, M. Melo, T. Catarino, J. Lima, J. M. Lopes, V. Máximo, M. Sobrinho-Simões, and P. Soares, "Telomerase promoter mutations in cancer: An emerging molecular biomarker?," *Virchows Arch*, Vol. 465, no. 2, pp. 119–33, 2014.

11. "Comprehensive, integrative genomic analysis of diffuse lower-grade gliomas," *New England Journal of Medicine*, Vol. 372, no. 26, pp. 2481–2498, 2015.

12. Yan, H., D. W. Parsons, G. Jin, R. McLendon, B. A. Rasheed, W. Yuan, I. Kos, I. Batinic-Haberle, S. Jones, G. J. Riggins, H. Friedman, A. Friedman, D. Reardon, J. Herndon, K. W. Kinzler, V. E. Velculescu, B. Vogelstein, and D. D. Bigner, "IDH1 and IDH2 mutations in gliomas," *New England Journal of Medicine*, Vol. 360, no. 8, pp. 765–773, 2009. PMID: 19228619.

13. Killela, P. J., C. J. Pirozzi, P. Healy, Z. J. Reitman, E. Lipp, A. B. Rasheed, R. Yang, B. H. Diplas, Z. Wang, P. K. Greer, H. Zhu, C. Y. Wang, A. B. Carpenter, H. Friedman, A. H. Friedman, S. T. Keir, J. He, Y. He, R. E. McLendon, J. E. Herndon II, H. Yan, and D. D. Bigner, "Mutations in idh1, idh2, and in the tert promoter define clinically distinct subgroups of adult malignant gliomas," *Oncotarget*, Vol. 5, no. 6, pp. 1515–1525, 2014.

14. Barbaro, M., H. A. Fine, and R. S. Magge, "Scientific and clinical challenges within neuro–oncology," *World Neurosurgery*, 2021.

15. Tozer, D. J., H. R. Jäger, N. Danchaivijitr, C. E. Benton, P. S. Tofts, J. H. Rees, and A. D. Waldman, "Apparent diffusion coefficient histograms may predict low-grade glioma subtype," *NMR in Biomedicine*, Vol. 20, no. 1, pp. 49–57, 2007.

16. Pope, W. B., X. J. Qiao, H. J. Kim, A. Lai, P. Nghiemphu, X. Xue, B. M. Ellingson, D. Schiff, D. Aregawi, S. Cha, V. K. Puduvalli, J. Wu, W.-K. A. Yung, G. S. Young, J. Vredenburgh, D. Barboriak, L. E. Abrey, T. Mikkelsen, R. Jain, N. A. Paleologos, P. L. RN, M. Prados, J. Goldin, P. Y. Wen, and T. Cloughesy, "Apparent diffusion coefficient histogram analysis stratifies progression–free and overall survival in patients with recurrent GBM treated with bevacizumab: A multi-center study," *Journal of Neuro-Oncology*, Vol. 108, no. 3, pp. 491–498, 2012.

17. Ozturk-Isik, E., A. Pirzkall, K. R. Lamborn, S. Cha, S. M. Chang, and S. J. Nelson, "Spatial characteristics of newly diagnosed grade 3 glioma assessed by magnetic resonance metabolic and diffusion tensor imaging," *Translational Oncology*, Vol. 5, no. 1, pp. 10 – 18, 2012.

18. Maynard, J., S. Okuchi, S. Wastling, A. A. Busaidi, O. Almossawi, W. Mbatha, S. Brandner, Z. Jaunmuktane, A. M. Koc, L. Mancini, R. Jäger, and S. Thust, "World health organization grade II/III glioma molecular status: Prediction by MRI morphologic features and apparent diffusion coefficient," *Radiology*, Vol. 296, no. 1, pp. 111–121, 2020. PMID: 32315266.

19. Sahm, F., D. Capper, A. Jeibmann, A. Habel, W. Paulus, D. Troost, and A. von Deimling, "Addressing diffuse glioma as a systemic brain disease with single-cell analysis," *Archives of Neurology*, Vol. 69, pp. 523–526, 04 2012.

20. Scherer, H. J., "Structural development in gliomas," *The American Journal of Cancer*, Vol. 34, no. 3, pp. 333–351, 1938.

21. Mohsen, L. A., V. Shi, R. Jena, J. H. Gillard, and S. J. Price, "Diffusion tensor invasive phenotypes can predict progression–free survival in glioblastomas," *British Journal of Neurosurgery*, Vol. 27, no. 4, pp. 436–441, 2013.

22. Esmaeili, M., A. L. Stensjøen, E. M. Berntsen, O. Solheim, and I. Reinertsen, "The direction of tumour growth in glioblastoma patients," *Scientific Reports*, Vol. 8, no. 1, p. 1199, 2018.

23. Zhang, F., J. Xie, G. Liu, Y. He, G. Lu, and X. Chen, "In vivo mri tracking of cell invasion and migration in a rat glioma model," *Molecular Imaging and Biology*, Vol. 13, no. 4, pp. 695–701, 2011.

24. Scherer, H. J., "The forms of growth in gliomas and their practical significance," *Brain*, Vol. 63, pp. 1–35, 03 1940.

25. Bølge Tysnes, B., and R. Mahesparan, "Biological mechanisms of glioma invasion and potential therapeutic targets," *Journal of Neuro-Oncology*, Vol. 53, no. 2, pp. 129–147, 2001.

26. Zetterling, M., K. R. Roodakker, S. G. Berntsson, P.-H. Edqvist, F. Latini, A.-M. Landtblom, F. Pontén, I. Alafuzoff, E.-M. Larsson, and A. Smits, "Extension of diffuse low–grade gliomas beyond radiological borders as shown by the coregistration of histopathological and magnetic resonance imaging data," *Journal of Neurosurgery JNS*, Vol. 125, no. 5, pp. 1155 – 1166, 2016.

27. Basser, P., J. Mattiello, and D. LeBihan, "Estimation of the effective self–diffusion tensor from the NMR spin echo," *Journal of Magnetic Resonance, Series B*, Vol. 103, no. 3, pp. 247 – 254, 1994.

28. Basser, P. J., "Inferring microstructural features and the physiological state of tissues from diffusion-weighted images," *NMR in Biomedicine*, Vol. 8, no. 7, pp. 333–344, 1995.

29. Basser, P. J., and C. Pierpaoli, "Microstructural and physiological features of tissues elucidated by quantitative–diffusion–tensor MRI," *Journal of Magnetic Resonance, Series B*, Vol. 111, no. 3, pp. 209 – 219, 1996.

30. Price, S., N. Burnet, T. Donovan, H. Green, A. Peña, N. Antoun, J. Pickard, T. Carpenter, and J. Gillard, "Diffusion tensor imaging of brain tumours at 3T: A potential tool for assessing white matter tract invasion?," *Clinical Radiology*, Vol. 58, no. 6, pp. 455–462, 2003.

31. Inglese, M., S. Brown, G. Johnson, M. Law, E. Knopp, and O. Gonen, "Whole–brain N–acetylaspartate spectroscopy and diffusion tensor imaging in patients with newly diagnosed gliomas: A preliminary study," *American Journal of Neuroradiology*, Vol. 27, no. 10, pp. 2137–2140, 2006.

32. Maudsley, A. A., B. Roy, R. K. Gupta, S. Sheriff, R. Awasthi, M. Gu, N. Husain, S. Mohakud, S. Behari, and D. M. Spielman, "Association of metabolite concentrations and water diffusivity in normal appearing brain tissue with glioma grade," *Journal of Neuroimaging*, Vol. 24, no. 6, pp. 585–589, 2014.

33. Goebell, E., J. Fiehler, X.-Q. Ding, S. Paustenbach, S. Nietz, O. Heese, T. Kucinski, C. Hagel, M. Westphal, and H. Zeumer, "Disarrangement of fiber tracts and decline of neuronal density correlate in glioma patients–a combined diffusion tensor imaging and 1h-mr spectroscopy study," *American Journal of Neuroradiology*, Vol. 27, no. 7, pp. 1426–1431, 2006.

34. Kallenberg, K., T. Goldmann, J. Menke, H. Strik, H. C. Bock, A. Mohr, J. H. Buhk, J. Frahm, P. Dechent, and M. Knauth, "Abnormalities in the normal appearing white matter of the cerebral hemisphere contralateral to a malignant brain tumor detected by diffusion tensor imaging," *Folia Neuropathol*, Vol. 52, no. 3, pp. 226–33, 2014.

35. Provenzale, J. M., P. McGraw, P. Mhatre, A. C. Guo, and D. Delong, "Peritumoral brain regions in gliomas and meningiomas: Investigation with isotropic diffusion-weighted MR imaging and diffusion-tensor MR imaging," *Radiology*, Vol. 232, no. 2, pp. 451–460, 2004. PMID: 15215555.

36. Horváth, A., G. Perlaki, A. Tóth, G. Orsi, S. Nagy, T. Dóczi, Z. Horváth, and P. Bogner, "Increased diffusion in the normal appearing white matter of brain tumor patients: Is this just tumor infiltration?," *Journal of Neuro-Oncology*, Vol. 127, pp. 83–90, Mar 2016.

37. Kassubek, R., M. Gorges, M.-A. Westhoff, A. C. Ludolph, J. Kassubek, and H.-P. Müller, "Cerebral microstructural alterations after radiation therapy in high–grade glioma: A diffusion tensor imaging–based study," *Frontiers in Neurology*, Vol. 8, p. 286, 2017.

38. Stadlbauer, A., O. Ganslandt, R. Buslei, T. Hammen, S. Gruber, E. Moser, M. Buchfelder, E. Salomonowitz, and C. Nimsky, "Gliomas: Histopathologic evaluation of changes in directionality and magnitude of water diffusion at diffusion-tensor mr imaging," *Radiology*, Vol. 240, no. 3, pp. 803–810, 2006. PMID: 16926329.

39. Deng, Z., Y. Yan, D. Zhong, G. Yang, W. Tang, F. Lü, B. Xie, and B. Liu, "Quantitative analysis of glioma cell invasion by diffusion tensor imaging," *Journal of Clinical Neuroscience*, Vol. 17, no. 12, pp. 1530–1536, 2010.

40. Jütten, K., V. Mainz, S. Gauggel, H. J. Patel, F. Binkofski, M. Wiesmann, H. Clusmann, and C.-H. Na, "Diffusion tensor imaging reveals microstructural heterogeneity of normal–appearing white matter and related cognitive dysfunction in glioma patients," *Frontiers in Oncology*, Vol. 9, p. 536, 2019.

41. Price, S. J., K. Allinson, H. Liu, N. R. Boonzaier, J.-L. Yan, V. C. Lupson, and T. J. Larkin, "Less invasive phenotype found in isocitrate dehydrogenase–mutated glioblastomas than in isocitrate dehydrogenase wild-type glioblastomas: A diffusion-tensor imaging study," *Radiology*, Vol. 283, no. 1, pp. 215–221, 2017. PMID: 27849434.

42. Aliotta, E., P. P. Batchala, D. Schiff, B. M. Lopes, J. T. Druzgal, S. Mukherjee, and S. H. Patel, "Increased intratumoral infiltration in idh wild-type lower-grade gliomas observed with diffusion tensor imaging," *Journal of Neuro-Oncology*, Vol. 145, no. 2, pp. 257–263, 2019.

43. Pope, W. B., H. J. Kim, J. Huo, J. Alger, M. S. Brown, D. Gjertson, V. Sai, J. R. Young, L. Tekchandani, T. Cloughesy, P. S. Mischel, A. Lai, P. Nghiemphu, S. Rahmanuddin, and J. Goldin, "Recurrent glioblastoma multiforme: ADC histogram analysis predicts response to bevacizumab treatment," *Radiology*, Vol. 252, no. 1, pp. 182–189, 2009. PMID: 19561256.

44. Pope, W., A. Lai, R. Mehta, H. Kim, J. Qiao, J. Young, X. Xue, J. Goldin, M. Brown, P. Nghiemphu, A. Tran, and T. Cloughesy, "Apparent diffusion coefficient histogram analysis stratifies progression-free survival in newly diagnosed bevacizumab-treated glioblastoma," *American Journal of Neuroradiology*, Vol. 32, no. 5, pp. 882–889, 2011.

45. Ellingson, B., S. Sahebjam, H. Kim, W. Pope, R. Harris, D. Woodworth, A. Lai, P. Nghiemphu, W. Mason, and T. Cloughesy, "Pretreatment ADC histogram analysis is a predictive imaging biomarker for bevacizumab treatment but not chemotherapy in recurrent glioblastoma," *American Journal of Neuroradiology*, Vol. 35, no. 4, pp. 673–679, 2014.

46. Ellingson, B. M., E. R. Gerstner, M. Smits, R. Y. Huang, R. Colen, L. E. Abrey, D. T. Aftab, G. M. Schwab, C. Hessel, R. J. Harris, A. Chakhoyan, R. Gahrmann, W. B. Pope, K. Leu, C. Raymond, D. C. Woodworth, J. de Groot, P. Y. Wen, T. T. Batchelor, M. J. van den Bent, and T. F. Cloughesy, "Diffusion MRI phenotypes predict overall survival benefit from anti–VEGF monotherapy in recurrent glioblastoma: Converging evidence from phase II trials," *Clinical Cancer Research*, Vol. 23, no. 19, pp. 5745–5756, 2017.

47. Patel, K. S., R. G. Everson, J. Yao, C. Raymond, J. Goldman, J. Schlossman, J. Tsung, C. Tan, W. B. Pope, M. S. Ji, N. T. Nguyen, A. Lai, P. L. Nghiemphu, L. M. Liau, T. F. Cloughesy, and B. M. Ellingson, "Diffusion magnetic resonance imaging phenotypes predict overall survival benefit from bevacizumab or surgery in recurrent glioblastoma with large tumor burden," *Neurosurgery*, Vol. 87, pp. 931–938, 05 2020.

48. Huo, J., H. J. Kim, W. B. Pope, K. Okada, J. R. Alger, Y. Wang, J. G. Goldin, and M. S. Brown, "Histogram–based classification with Gaussian mixture modeling for GBM tumor treatment response using ADC map," in *Medical Imaging 2009: Computer-Aided Diagnosis* (Karssemeijer, N., and M. L. Giger, eds.), Vol. 7260, pp. 566 – 572, International Society for Optics and Photonics, SPIE, 2009.

49. Lutz, K., B. Wiestler, M. Graf, P. Bäumer, R. Floca, H.-P. Schlemmer, S. Heiland, W. Wick, M. Bendszus, and A. Radbruch, "Infiltrative patterns of glioblastoma: Identification of tumor progress using apparent diffusion coefficient histograms," *Journal of Magnetic Resonance Imaging*, Vol. 39, no. 5, pp. 1096–1103, 2014.

50. Ozturk-Isik, E., S. Cengiz, A. Ozcan, C. Yakicier, A. Ersen Danyeli, M. N. Pamir, K. Ozduman, and A. Dincer, "Identification of IDH and TERTp mutation status using 1H–MRS in 112 hemispheric diffuse gliomas," *Journal of Magnetic Resonance Imaging*, Vol. 51, no. 6, pp. 1799–1809, 2020.

51. Malaterre, M., "GDCM : Grassroots dicom library."

52. Bazin, P.-L., J. L. Cuzzocreo, M. A. Yassa, W. Gandler, M. J. McAuliffe, S. S. Bassett, and D. L. Pham, "Volumetric neuroimage analysis extensions for the MIPAV software package," *Journal of Neuroscience Methods*, Vol. 165, no. 1, pp. 111 – 121, 2007.

53. Jenkinson, M., C. F. Beckmann, T. E. Behrens, M. W. Woolrich, and S. M. Smith, "FSL," *NeuroImage*, Vol. 62, no. 2, pp. 782 – 790, 2012.

54. Zhang, Y., Y. Liu, and C.-H. Chen, "Review on deep learning in feature selection," in *The 10th International Conference on Computer Engineering and Networks* (Liu, Q., X. Liu, T. Shen, and X. Qiu, eds.), (Singapore), pp. 439–447, Springer Singapore, 2021.

55. Alpaydin, E., *Introduction to Machine Learning*, Adaptive Computation and Machine Learning series, MIT Press, 2014.

56. Kohavi, R., and G. H. John, "Wrappers for feature subset selection," *Artificial Intelligence*, Vol. 97, no. 1, pp. 273–324, 1997.

57. Guyon, I., "An introduction to variable and feature selection," *Journal of Machine Learning Research*, Vol. 3, pp. 1157–1182, 2003.

58. Long, C., "Visualization of matrix singular value decomposition," *Mathematics Magazine*, Vol. 56, no. 3, pp. 161–167, 1983.

59. Lay, D., S. Lay, and J. McDonald, *Linear Algebra and Its Applications*, Pearson, 2016.

60. Pedregosa, F., G. Varoquaux, A. Gramfort, V. Michel, B. Thirion, O. Grisel, M. Blondel, P. Prettenhofer, R. Weiss, V. Dubourg, J. Vanderplas, A. Passos, D. Cournapeau, M. Brucher, M. Perrot, and E. Duchesnay, "Scikit-learn: Machine learning in Python," *Journal of Machine Learning Research*, Vol. 12, pp. 2825–2830, 2011.

61. MathWorks, "Matlab 2021a curve fitting toolbox user's guide," 2021.

62. MathWorks, "Matlab 2021a optimization toolbox user's guide," 2021.

63. Bishop, C. M., *Pattern Recognition and Machine Learning*, Springer, 2006.

64. Glantz, S., *Primer of Biostatistics, Seventh Edition*, McGraw-Hill Education, 2011.

65. MathWorks, "Matlab 2021a statistics and machine learning toolbox user's guide," 2021.

66. Smialowski, P., D. Frishman, and S. Kramer, "Pitfalls of supervised feature selection," *Bioinformatics*, Vol. 26, pp. 440–443, 10 2009.

67. Seiffert, C., T. M. Khoshgoftaar, J. Van Hulse, and A. Napolitano, "Rusboost: Improving classification performance when training data is skewed," in *2008 19th International Conference on Pattern Recognition*, pp. 1–4, 2008.

68. Chawla, N. V., K. W. Bowyer, L. O. Hall, and W. P. Kegelmeyer, "Smote: Synthetic minority over–sampling technique," *Journal of Artificial Intelligence Research*, Vol. 16, pp. 321–357, Jun 2002.

69. Nekooeimehr, I., and S. K. Lai-Yuen, "Adaptive semi–unsupervised weighted oversampling (a-suwo) for imbalanced datasets," *Expert Systems with Applications*, Vol. 46, pp. 405–416, 2016.

70. Bzdok, D., N. Altman, and M. Krzywinski, "Statistics versus machine learning," *Nature Methods*, Vol. 15, no. 4, pp. 233–234, 2018.

71. Rosner, B., *Fundamentals of Biostatistics*, Cengage Learning, 2015.